Mechanism and Machine Theory 171 (2022) 104742

Contents lists available at ScienceDirect

Mechanism and Machine Theory

journal homepage: www.elsevier.com/locate/mechmt

Research paper

Panhead accelerations-based methodology for monitoring the stagger in overhead contact line systems

Blas Blanco [a,b,c,*], Itxaro Errandonea [b,c,**], Sergio Beltrán [b,c,d], Saioa Arrizabalaga [b,c,d], Unai Alvarado [b,c]

[a] Department of Mechanical and Production Engineering, Aarhus University, Inge Lehmanns Gade 10, 8000 Aarhus, Denmark
[b] CEIT-Basque Research and Technology Alliance (BRTA), Manuel Lardizabal 13, 20018 Donostia/San Sebastián, Spain
[c] Universidad de Navarra, Tecnun, Manuel Lardizabal 13, 20018 Donostia/San Sebastián, Spain
[d] Institute of Data Science and Artificial Intelligence, DATAI, Universidad de Navarra, Pamplona, Spain

ARTICLE INFO

Keywords:
Railway
Infrastructure monitoring
Pantograph–catenary interaction
Stagger
Virtual environment
Machine learning

ABSTRACT

The monitoring of overhead contact lines (OCL) is a key part of railway infrastructure maintenance. This paper proposes a methodology to assess the lateral geometry of contact wire, the so-called stagger, by using the dynamic response of a pantograph. The methodology is tested in a validated virtual environment that resembles the behaviour of the pantograph when it interacts with the OCL. A signal processing is developed to define features relating the lateral position of the contact wire with the vertical acceleration of the contact strip. It is demonstrated that these features have a clear and close connection with the lateral position of the contact wire. Subsequently, model-driven machine learning algorithms are defined using these features to address the OCL stagger prediction and the detection of out-of-range lateral displacement due to a faulty steady-arm. The methodology shows a good prediction performance in the estimation of the stagger amplitude/central position and the steady-arms diagnosis. The prediction of the stagger amplitude is performed with a root-mean-square error of 4.7(10) mm. In addition, the area under the Precision–Recall curve is 0.952 CI_{95} [0.940, 0.962] for the steady-arms diagnosis.

1. Introduction

The overhead contact line (OCL) is the infrastructure responsible for the energy supply in most electrified railway systems. Fig. 1(a) shows a scheme of a simple alternating current (AC) OCL type. Two main types of wires compose the OCL, the contact wire (CW), which directly interacts with the pantograph, and the messenger wire (MW), which bears the system weight and transmits it to the masts. Droppers are responsible for connecting both wires. On the vehicle side, a pantograph is mounted on the roof of the vehicle for collecting the energy supplied by the OCL (Fig. 1(b)). The pantograph is formed by articulated arms that are uplifted and pushed against the OCL by a drive. The upper part of the pantograph, the panhead, is formed by one or several contact strips that slide along the OCL.

Concerning contact strips, two parts are distinguishable in their design. The carrier, a metal skeleton generally made of aluminium that holds the second part, which is a carbon-based strip band designed to contact the CW. The CW material is a metal alloy, generally, CuAg made of. The sliding interaction between both contacting surfaces leads to a significant amount of wear that is mainly located at the contact strip side [1,2]. To achieve uniform wear of the contact strip, the CW follows a zig-zag lateral pattern,

* Corresponding author at: Department of Mechanical and Production Engineering, Aarhus University, Inge Lehmanns Gade 10, 8000 Aarhus, Denmark.
** Corresponding author at: CEIT-Basque Research and Technology Alliance (BRTA), Manuel Lardizabal 13, 20018 Donostia/San Sebastián, Spain.
E-mail addresses: blas@mpe.au.dk (B. Blanco), ierrandonea@ceit.es (I. Errandonea).

https://doi.org/10.1016/j.mechmachtheory.2022.104742
Received 6 October 2021; Received in revised form 10 January 2022; Accepted 15 January 2022
Available online 8 February 2022
0094-114X/© 2022 The Author(s). Published by Elsevier Ltd. This is an open access article under the CC BY license (http://creativecommons.org/licenses/by/4.0/).

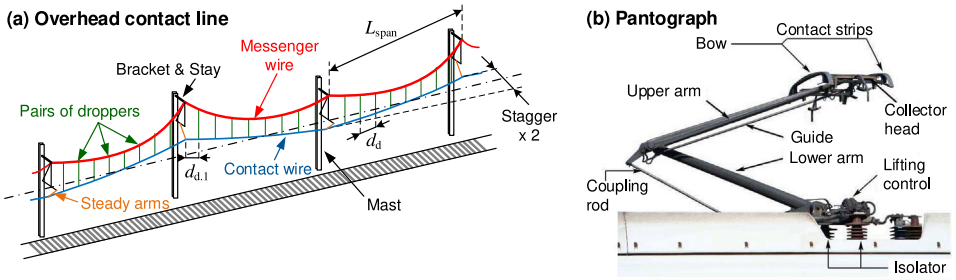

Fig. 1. Schematic representations of the overhead contact line (OCL) (a) and the pantograph (b).

known as stagger, that prevents from grooving. The stagger is provided by the steady-arms (SAs), which impose the lateral position while allowing vertical deflection. The maximum value of the stagger is constrained by safety reasons since an excessive stagger can lead to a pantograph dewirement, which in turn might result in the OCL destruction. Therefore, the stagger is one of the most important subjects of monitoring for infrastructure maintainers [3]. Some papers establish a further distinction between the stagger as measured when no vehicle is interacting with the OCL, and the resulting one when the pantograph interacts with it [4–6]. The latter is known as dynamic stagger, and it is the one considered in the present article.

In the last years, several approaches have been developed for dynamic stagger monitoring. Most of them are based on video processing methodologies [4,6,7]. They provide high accuracy and are contactless. A different approach is due to Bocciolone et al. [5,8] that uses force transducers based on fibre Bragg grating. The trace of the stagger is significant in force measurements at a frequency dependent on the vehicle speed, and a distance equals to twice the mast separation. At most, the corresponding frequency is slightly higher than 1 Hz. The methodology of Bocciolone et al. [5,8] measures the force due to contact and strip supports. Subsequently, by applying moment equilibrium, the force application position is estimated, *i.e.* the dynamic stagger. The latter methodology, which uses signal processing instead of video analysis, has the main advantage of requiring much less computational effort.

Fibre Brag grating is intended to replace traditional electrical sensor set-ups [9]. The disadvantage of electrical sensors is that they have to deal with electrical insulation issues. Nonetheless, electrical measurement set-ups like those based on capacitive accelerometers are more affordable in economic terms [5]. Therefore, acceleration signals obtained by traditional electrical sensors are still an interesting choice to monitor OCL status.

Concerning the OCL monitoring based on pantograph dynamics response, Carnevale et al. [10], Song et al. [11,12] and Wang et al. [13] propose methodologies based on the analysis of panhead accelerations to detect local OCL defects. Another application is due to Wang et al. [14] for the identification of characteristic structure wavelengths. However, under the authors' knowledge, there are no previous attempts to estimate the stagger based on the acceleration response of the pantograph. Probably, this is due to the fact that the stagger frequency acts in a low-frequency range, where the dynamic response has an almost negligible magnitude. Therefore, inertial measurements are not often considered suitable for stagger estimation.

This paper tackles this gap in the state-of-the-art by proposing a methodology for the OCL stagger estimation based on the dynamic response of the pantograph, concretely, the vertical contact strip accelerations. The proposal uses data simulated in a virtual environment recreating the pantograph-OCL interaction, which is validated by the standard EN-50318-2018 [15]. This standard establishes a range of validation from 0 Hz to 20 Hz, but it can be extended by including a more detailed description of the pantograph [16], and by a careful selection of the contact coefficients, the time-step length and the finite element mesh [17,18]. The validity of the methodology is further guaranteed by considering diverse sources of structural uncertainties and analysing its performance in low, medium and high speeds conditions. The analysis of the panhead accelerations relies on the Continuous Wavelet Transform (CWT), which has been previously used in OCL studies [11,13,14,19]. More specifically, a strong relation between OCL stagger and panhead accelerations is revealed by the Scale Average Wavelet Power (SAWP) [20]. Signal processing based on SAWP is applied successfully by Molodova et al. [21] on the rail surface defects detection. The proposed methodology takes advantage of the impact of stagger on SAWP results. It defines variable predictors of the OCL that machine learning models employ in the stagger monitoring and diagnosis. In this regard, the virtual environment is used to generate training and validation datasets. They encompass a comprehensive range of OCL lateral configurations and uncommon circumstances like those related to disturbed steady-arms.

The use of machine learning models for monitoring and diagnosing the stagger has been mainly constrained to artificial neural networks for image processing [6,22,23]. They monitor the contact point between the pantograph and the contact line. With the estimation of the contact point, the dynamic stagger can be predicted. The main disadvantage of these approaches is the computational cost of training convolutional neural networks together with a large number of human labelled images. This is also an issue for support vector machines when several features are extracted from images [4]. In order to overcome these drawbacks, a different approach is proposed in this article.

In recent years, an active field of research has developed around the progressive automation of machine learning. AutoML frameworks initially emerged so that novice users could create useful models, while experts could use them to speed up their tasks. Nonetheless, as machine learning pipelines are growing in complexity and computational cost, AutoML is becoming a

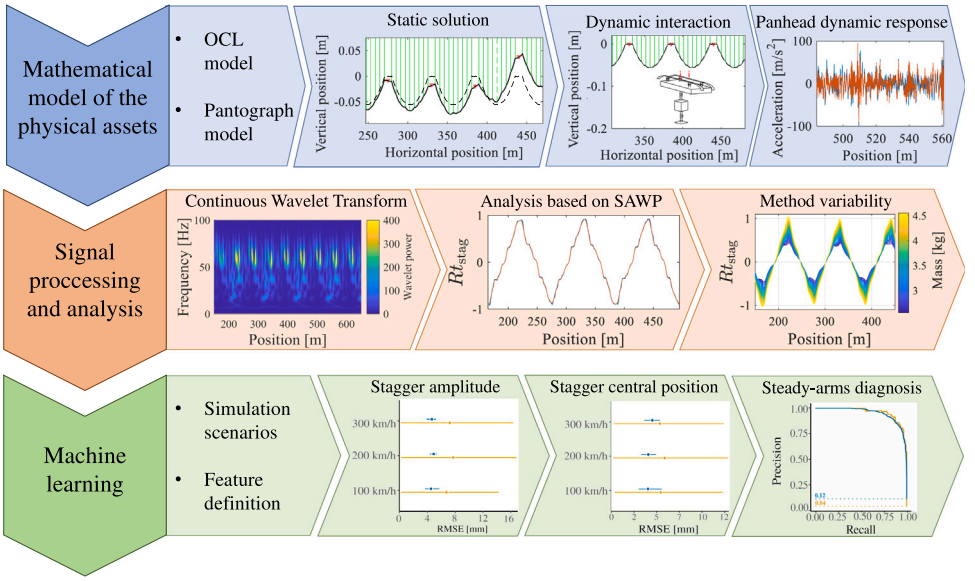

Fig. 2. Scheme of the proposed methodology.

complementary tool that leverages humans' combined domain and technical knowledge [24]. AutoML is quickly gaining ground in a wide range of industrial applications. Some examples can be seen in the fields of medical image classification [25], online travel mode detection [26] and customer delivery satisfaction [27].

The article proposes the use of AutoML frameworks for an accurate and efficient estimation of the stagger and the diagnosis of steady-arms. To the authors' knowledge, it is the first time that AutoML frameworks are applied for the health estimation of railway infrastructure. As a contribution to the state-of-the-art in the OCL monitoring, this article introduces the use of tabular machine learning models to estimate the stagger and diagnose of steady-arms by using time series characteristics extracted from accelerometers. The obtained results confirm the feasibility of this approach.

Fig. 2 outlines the structure of the paper, which is divided into three main parts. Firstly, the definition of the mathematical model employed to resemble real panhead accelerations (Section 2). Secondly, the description of the procedure for the signal processing based on CWT and SAWP (Section 3). It follows the analysis of the dependence of the proposed signal processing on speed, pantograph features and OCL geometrical uncertainties (Section 4). Thirdly, features are defined for the training of the machine learning algorithms and their performance is assessed (Section 5). Finally, the discussion and conclusions are presented in Sections 6 and 7, respectively.

2. Mathematical model of the OCL and pantograph

In this section, the mathematical modelling of the OCL structure is presented. Subsequently, the procedures to perform the initial static calculation and the dynamic interaction are exposed. In addition, the pantograph model is also explained.

2.1. OCL model description

There are several common configurations of OCL. The standard EN 50318-2018 [15] takes into account three types, simple and stitched AC OCL and double contact wire OCL. In this study, the simple AC OCL is used to reproduce the dynamic pantograph-OCL interaction. Nevertheless, the conclusions drawn by this work apply to other OCL types. Fig. 1(a) shows a graphical representation of the simple AC OCL type.

Concerning the mathematical modelling, the CW and MW are modelled with Euler–Bernoulli beam finite elements (FE). Most models included in the benchmark presented by Bruni et al. [28] use this choice. Nevertheless, if large deformations occur, the absolute nodal coordinate formulation [29–31] is a more suitable choice. The stiffening of the wires due to tensioning devices is included by adding a geometric stiffness matrix. The elementary matrices definitions can be found in [32]. The mesh uses 20 and 10 FE to describe CW and MW sections between adjacent droppers, respectively. This configuration guarantees the validity of the model up to about 93 Hz, 185 Hz and 278 Hz for speeds of 100 km/h, 200 km/h and 300 km/h, respectively. Bar elements with zero stiffness under compression model the droppers. These components are responsible for the non-linear behaviour of the OCL structure. At the joining positions between wires and droppers, masses should be introduced to account for clamping elements. Concerning the masts, they can be represented as high stiffness elements constraining the vertical motion of the MW. The SA is introduced here as a mass–spring element. All the parameters required for the formulation of the OCL are taken from the standard EN 50318-2018 [15].

The OCL model is formulated as a 2D system that neglects lateral OCL dynamics. This choice is justified for several reasons. Firstly, the proposed methodology only uses the pantograph vertical response, which is not thought to be highly affected by OCL lateral dynamics. Secondly, the benchmarked models in Bruni et al. [28] show a reduced impact of considering lateral dynamics on the contact force up to 20 Hz. Therefore, although some results differences might be expected if considering lateral dynamics, the main conclusions should not lose their validity. And thirdly, the benefits of implementing OCL lateral dynamics do not seem to be worth the involved computational cost, which is an important matter when dealing with machine learning algorithms.

Despite neglecting the lateral OCL dynamics, the pantograph vertical response accounts for the OCL lateral geometry. This is achieved by shifting the contact forces acting positions along the pantograph strips accordingly to the lateral geometry imposed by the stagger. This approach is also used in 2D OCL models by Cho [33].

2.2. Initial static problem

The calculus of the static problem refers to those procedures intended to obtain the deformed position of the OCL under gravitational load, and the extraction of non-defined parameters to meet with the required initial position. The latter is the case of the simple AC OCL defined in EN-50318-2018 [15]. The specifications refer to the height of the CW at dropper positions. The dropper lengths must be calculated such that they meet that requirement. In this work, a similar procedure to the one explained by Ikeda [34] is followed. Firstly, Ikeda [34] calculates the necessary dropper forces to obtain the desired initial position. Once these forces are known, the initial position of the MW and CW are calculated. Subsequently, the length of each dropper is derived, which enables the calculation of the dropper stiffness as

$$k_{\mathrm{d}.d} = E_{\mathrm{d}} A_{\mathrm{d}} / L_{\mathrm{d}.d}, \tag{1}$$

where A_{d} is the cross-sectional area of the dropper, E_{d} is the dropper Young's modulus and $L_{\mathrm{d}.d}$ is the length of the dth dropper. After obtaining the droppers stiffness, the dropper stiffness matrix, $\mathbf{K}_{\mathrm{d}}$, is built using bar elements. The matrix $\mathbf{K}_{\mathrm{d}}$ is responsible for the coupling of $\mathbf{K}_{\mathrm{MW}}$ and $\mathbf{K}_{\mathrm{CW}}$, the MW and CW stiffness matrices, respectively. The static equilibrium of the OCL reads

$$\begin{bmatrix} \mathbf{K}_{\mathrm{MW}} + \mathbf{K}_{\mathrm{d.MW}} & \mathbf{K}_{\mathrm{d.cross}} \\ \mathbf{K}_{\mathrm{d.cross}} & \mathbf{K}_{\mathrm{CW}} + \mathbf{K}_{\mathrm{d.CW}} \end{bmatrix} \begin{bmatrix} \mathbf{q}_{\mathrm{CW}} \\ \mathbf{q}_{\mathrm{MW}} \end{bmatrix} = \mathbf{K}_{\mathrm{c}} \mathbf{q}_{\mathrm{c}} = \mathbf{f}_{\mathrm{bal}} + \mathbf{f}_{\mathrm{g}}, \tag{2}$$

where $\mathbf{K}_{\mathrm{c}}$ and $\mathbf{q}_{\mathrm{c}}$ denote the stiffness matrix and generalized coordinates of the OCL, respectively (subscript 'c' refers to catenary), and $\mathbf{f}_{\mathrm{g}}$ contains the gravity loads. The vector $\mathbf{f}_{\mathrm{bal}} = \mathbf{f}_{\mathrm{bal.s}} + \mathbf{f}_{\mathrm{bal.d}}$, being $\mathbf{f}_{\mathrm{bal.s}} = \mathbf{b}_{\mathrm{s}} h_{\mathrm{mast}} k_{\mathrm{s}}$ and $\mathbf{f}_{\mathrm{bal.d}} = \mathbf{K}_{\mathrm{d}} \mathbf{L}_{\mathrm{d}}$. The vectors $\mathbf{f}_{\mathrm{bal.s}}$ and $\mathbf{f}_{\mathrm{bal.d}}$ are the balancing forces of the mast supports and droppers, respectively. They impose the initial state at both components. The mast support stiffness is denoted as k_{s}, $\mathbf{b}_{\mathrm{s}}$ is a Boolean vector with non-zero values at the vertical degrees of freedom (DoF) corresponding to the mast supports, h_{mast} is the MW height at the mast in relation to the CW, and $\mathbf{L}_{\mathrm{d}}$ introduces the initial elongation of droppers to the bar elements.

Up to this point, the calculation concerns the nominal definition of the OCL. However, there are geometrical uncertainties that affect both static and dynamic results. The pantograph-OCL dynamic interaction is affected most by the departure of the dropper length and the mast height from their nominal values [35]. The deviation in mast height is introduced into h_{mast}, which becomes a vector since each mast turns to have a different height. Regarding deviations in dropper lengths, it forces the redefinition of $\mathbf{K}_{\mathrm{d}}$ and $\mathbf{L}_{\mathrm{d}}$.

2.3. Pantograph model description

The modelling of the pantograph is addressed in two directions. Firstly, the lower part of the structure, which encompasses the upper and lower arms, is considered using a lumped mass model. Secondly, the panhead, formed by the contact strips and the elastic elements attaching strips to the upper arm. Concerning contact strips, solid rigid and flexible vibration modes describe their motion. Elements attaching the contact strips to the upper arm are modelled as Kelvin–Voigt interactions, with stiffness k_3 and viscous damping c_3. A FE model obtains the contact strip flexible vibration modes by using Euler–Bernoulli beam FEs.

The pantograph model scheme is shown in Fig. 3(a). The parameters of the lumped mass model are taken from the standard [15], with some modifications. Changes affect, firstly, the terms k_3 and c_3, which are divided by four to share out their contributions among the attachment positions, and secondly, m_3 and I_3, whose values are obtained by the FE model resulting in 3.9 kg and $0.65\,\mathrm{kg\,m^2}$, respectively.

Fig. 3(b) depicts the shape of the modelled pantograph contact strips. There are three main parts, two lateral horns, the central graphite strip and the central carrier. Horns and the central carrier are formed by a extrude beam made of the same material. Fig. 3(c) shows the normalized modal shapes of the contact strips along the length of the graphite strip. Only are represented those modal shapes whose corresponding natural frequency is below 300 Hz. The length of the graphite strip and the width of the pantograph contact strips are set in 1.11 m and 1.62 m, respectively. It is assumed that horns have quarter circular shapes. The cross-sectional data necessary for the formulation of the FE is given in Table 1.

Regarding the lumped mass model, the static force applied at the lowest lumped mass, f_{sta}, is responsible for keeping the contact force around its nominal value. It is calculated as indicated by the standard EN-50367 [36] as

$$f_{\mathrm{sta}} = 9.7 \cdot 10^{-4} V^2 + 70 \quad \text{in} \quad [\mathrm{N}], \tag{3}$$

where V [km/h] is the pantograph forward speed.

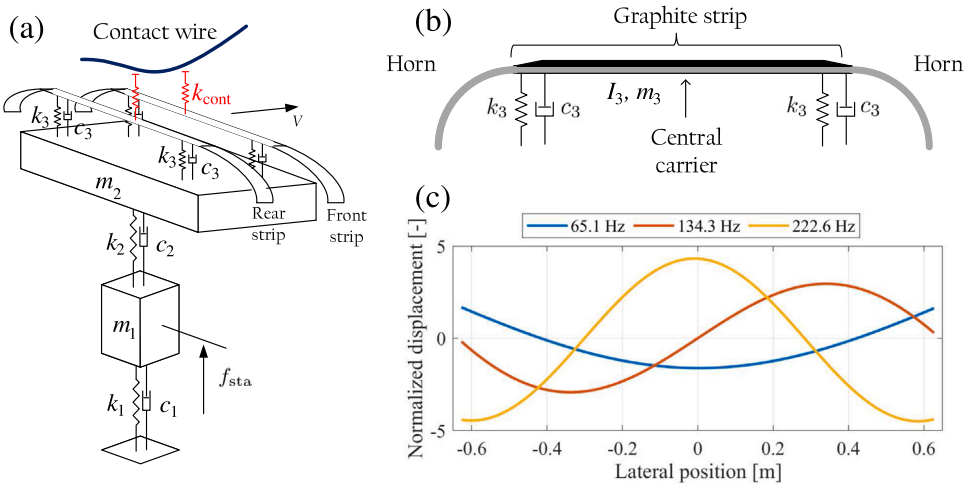

Fig. 3. (a) View of the lumped mass model of the pantograph. (b) Scheme of the contact strip implemented design. (c) Normalized modal shapes of the contact strips vibration modes.

Table 1
Mechanical and geometrical properties of the pantograph contact strips.

	Young's modulus (GPa)	Density (kg/m^3)	Height (mm)	Width (mm)	Thickness (mm)
Graphite	12.7	2000	20	60	–
Aluminium	68	2700	22	60	3

The generalized coordinates defining the pantograph motion are

$$\mathbf{q}_\mathrm{p} = \begin{bmatrix} w_1 & w_2 & w_{3,\mathrm{t}} & \theta_{3,\mathrm{t}} & \boldsymbol{\eta}_\mathrm{t} & w_{3,\mathrm{l}} & \theta_{3,\mathrm{l}} & \boldsymbol{\eta}_\mathrm{l} \end{bmatrix}, \tag{4}$$

where 't' and 'l' refer to the trailing and leading contact strips, respectively. The lumped mass displacements are w_1, w_2 and w_3, and the strip rotation is θ_3. The vector $\boldsymbol{\eta}$ includes the modal coordinates of the strips.

The mass matrix of the system simply reads

$$\mathbf{M}_\mathrm{p} = \mathrm{diag}\left(\begin{bmatrix} m_1 & m_2 & m_3 & I_3 & \mathbf{1} & m_3 & I_3 & \mathbf{1} \end{bmatrix}\right), \tag{5}$$

where the operator 'diag' builds a diagonal matrix. Since the flexible modal shapes are obtained under free boundary conditions, they are orthogonal to rigid body motions, leading to uncoupled rigid and flexible motions. The normalization of the modal shapes results in the identity matrix describing their inertia.

The pantograph stiffness matrix is defined by using the minimum potential energy principle as

$$\mathbf{K}_\mathrm{p} = \begin{bmatrix} k_1 & -k_2 & 0 & \cdots & 0 \\ -k_2 & k_2 & 0 & & \vdots \\ 0 & 0 & \mathbf{0}_{2\times2} & \ddots & \vdots \\ \vdots & & \ddots & \boldsymbol{\omega}^2 & \ddots \\ 0 & \cdots & \cdots & \ddots & 0 \\ & & & & \boldsymbol{\omega}^2 \end{bmatrix} + k_3 \sum_{i=\mathrm{t,l}} \sum_{j=1,2} \mathbf{N}_{ij}^\mathrm{T} \mathbf{N}_{ij}, \tag{6}$$

where

$$\mathbf{N}_{\mathrm{t},j} = \begin{bmatrix} 0 & 0 & 1 & y_{\mathrm{cs},j} & \mathbf{S}(y_{\mathrm{cs},j}) & \mathbf{0} \end{bmatrix}, \tag{7}$$

$$\mathbf{N}_{\mathrm{l},j} = \begin{bmatrix} 0 & 0 & \mathbf{0} & 1 & y_{\mathrm{cs},j} & \mathbf{S}(y_{\mathrm{cs},j}) \end{bmatrix}, \tag{8}$$

which multiplied by $\mathbf{q}_\mathrm{p}$ yield the relative displacement of the jth attachment. The vector $\mathbf{S}(y_\mathrm{cs})$ contains the contact strip modal shape values at y_cs, which is the lateral position measured from the centre of the contact strip. Because of the modal shape normalization, $\boldsymbol{\omega}^2 = \mathrm{diag}\left(\begin{bmatrix} \omega_1^2 & \cdots & \omega_{N_\mathrm{m}}^2 \end{bmatrix}\right)$, where N_m is the number of modes introduced at each strip. The pantograph damping matrix, $\mathbf{C}_\mathrm{p}$, has an analogous definition to $\mathbf{K}_\mathrm{p}$.

2.4. OCL-pantograph dynamic interaction

The dynamic formulation of the OCL requires the assembly of MW, CW and droppers mass matrices, $\mathbf{M}_{\mathrm{CW}}$, $\mathbf{M}_{\mathrm{MW}}$ and $\mathbf{M}_{\mathrm{d}}$, respectively, which should also include the inertia terms of clamping devices and SAs. In general terms, the definition of $\mathbf{M}_{\mathrm{c}}$ is analogous to that of $\mathbf{K}_{\mathrm{c}}$ pointed out in Eq. (2). Regarding the damping matrix, it is defined assuming proportional damping type as

$$\mathbf{C}_{\mathrm{c}} = \alpha_{\mathrm{c}}\mathbf{M}_{\mathrm{c}} + \beta_{\mathrm{c}}\mathbf{K}_{\mathrm{c}}, \tag{9}$$

where α_{c} and β_{c} are experimental OCL damping parameters, which are given in EN-50318-2018 [15].

In order to solve the OCL-pantograph interaction problem, the coupling between pantograph and OCL must be defined. The coupling is due to contact forces and it is modelled with a penalty method, as shown in Fig. 3(a), in which the ith contact force reads

$$f_{\mathrm{cont}.c} = \begin{cases} k_{\mathrm{cont}}\delta_c & \text{if} \quad \delta_c > 0 \\ 0 & \text{if} \quad \delta_c \leq 0, \end{cases} \tag{10}$$

where k_{cont} is a contact stiffness and $\delta_c = w_{\mathrm{p}.c} - w_{\mathrm{c}.c} - w_{\mathrm{irr}.c}$, being $w_{\mathrm{c}.c}$ and $w_{\mathrm{p}.c}$ the vertical displacements of CW and pantograph at the cth contact position, respectively, and w_{irr} introduces surface irregularities. If $\delta_c \leq 0$, a contact loss takes place and the contact force vanishes, which introduces a non-linear behaviour in the problem. The contact stiffness is set in 3 MN/m, which is in accordance with the order of magnitude predicted by the Hertzian theory [18].

The other source of non-linearities is due to the droppers, which in practice present an almost null stiffness when they are under compression. This behaviour is known as slackening. Similarly to the contact problem, slackening is modelled with a bi-linear stiffness. The elastic force of each dropper reads

$$f_{\mathrm{d}.d} = \begin{cases} k_{\mathrm{d}.d}\left(w_{\mathrm{d}.d}^{\mathrm{MW}} - w_{\mathrm{d}.d}^{\mathrm{CW}} - L_{\mathrm{d}.d}\right) & \text{if axially loaded} \\ 0 & \text{if slackening,} \end{cases} \tag{11}$$

where $w_{\mathrm{d}.d}^{\mathrm{MW}}$ and $w_{\mathrm{d}.d}^{\mathrm{CW}}$ are the vertical displacements of MW and CW at the clamping positions of the dth dropper, respectively. The system of equations introduces the dropper slackening by balance forces, $\mathbf{f}_{\mathrm{sd}}$, that make zero the elastic force due to slackened droppers. In this way, the system matrices become invariant, avoiding continuous redefinition of the Jacobian matrix. The system of equations to be solved reads

$$\begin{bmatrix} \mathbf{M}_{\mathrm{c}} & \mathbf{0} \\ \mathbf{0} & \mathbf{M}_{\mathrm{p}} \end{bmatrix} \begin{bmatrix} \ddot{\mathbf{q}}_{\mathrm{c}} \\ \ddot{\mathbf{q}}_{\mathrm{p}} \end{bmatrix} + \begin{bmatrix} \mathbf{C}_{\mathrm{c}} & \mathbf{0} \\ \mathbf{0} & \mathbf{C}_{\mathrm{p}} \end{bmatrix} \begin{bmatrix} \dot{\mathbf{q}}_{\mathrm{c}} \\ \dot{\mathbf{q}}_{\mathrm{p}} \end{bmatrix} + \begin{bmatrix} \mathbf{K}_{\mathrm{c}} & \mathbf{0} \\ \mathbf{0} & \mathbf{K}_{\mathrm{p}} \end{bmatrix} \begin{bmatrix} \mathbf{q}_{\mathrm{c}} \\ \mathbf{q}_{\mathrm{p}} \end{bmatrix} = \begin{bmatrix} \mathbf{f}_{\mathrm{bal}} + \mathbf{f}_{\mathrm{g}} + \mathbf{f}_{\mathrm{cont.c}} + \mathbf{f}_{\mathrm{sd}} \\ \mathbf{f}_{\mathrm{sta}} + \mathbf{f}_{\mathrm{cont.p}} \end{bmatrix}, \tag{12}$$

where $\mathbf{f}_{\mathrm{sta}}$ includes the upward lifting force of the pantograph defined by Eq. (3). The vectors $\mathbf{f}_{\mathrm{cont.c}}$ and $\mathbf{f}_{\mathrm{cont.p}}$ are the projections of the contact forces over the OCL and pantograph structures, respectively; which are responsible for the coupling between them. The Eq. (12) is further compacted leading to

$$\mathbf{M}_{\mathrm{sys}}\ddot{\mathbf{q}}_{\mathrm{sys}.t} + \mathbf{C}_{\mathrm{sys}}\dot{\mathbf{q}}_{\mathrm{sys}.t} + \mathbf{K}_{\mathrm{sys}}\mathbf{q}_{\mathrm{sys}.t} = \mathbf{f}_{\mathrm{sta.sys}} + \mathbf{f}_{\mathrm{cont.sys}} + \mathbf{f}_{\mathrm{sd.sys}}, \tag{13}$$

where $\mathbf{q}_{\mathrm{sys}.t}$ is the vector containing the unknown generalized coordinates of the system at the instant t. The vectors $\mathbf{f}_{\mathrm{bal}}$, $\mathbf{f}_{\mathrm{g}}$ and $\mathbf{f}_{\mathrm{sta}}$ are time independent, and are grouped into $\mathbf{f}_{\mathrm{sta.sys}}$. By using a second-order numerical integration method, the time derivatives of $\mathbf{q}_{\mathrm{sys}.t}$ in Eq. (12) can be written in terms of the their value in the previous instant, which leads to a general expression such as

$$\mathbf{K}_{\mathrm{Int}}\mathbf{q}_{\mathrm{sys}.t} = \mathbf{M}_{\mathrm{sys}}\hat{\ddot{\mathbf{q}}}_{t-\Delta t} + \mathbf{C}_{\mathrm{sys}}\hat{\dot{\mathbf{q}}}_{t-\Delta t} + \mathbf{f}_{\mathrm{sta.sys}} + \mathbf{f}_{\mathrm{cont.sys}} + \mathbf{f}_{\mathrm{sd.sys}}, \tag{14}$$

where Δt is the time-step and $\mathbf{q}_{\mathrm{sys}.t}$ is defined in term of the kinematic solution at the previous instant, $t - \Delta t$, whose influence is introduced by $\hat{\ddot{\mathbf{q}}}_{t-\Delta t}$ and $\hat{\dot{\mathbf{q}}}_{t-\Delta t}$. The definition of these terms, as well as $\mathbf{K}_{\mathrm{Int}}$, depends on the employed numerical integrator. Their definitions are included in Appendix A according to the numerical integrator based on the Newmark's method, which is the most efficient choice according to Gregori et al. [37]. The time step is set in 0.25 ms, which guarantees convergence of the solution in the high-frequency domain [17].

The large number of DoF of OCL models and the non-linear behaviour of $\mathbf{f}_{\mathrm{cont.sys}}$ and $\mathbf{f}_{\mathrm{sd.sys}}$ make the Newton–Raphson method an unsuitable choice to solve Eq. (14). This issue can be overcome by taking advantage of the bi-linear nature of these non-linearities as proposed by Gregori et al. [37]. In that methodology, the right-hand side of Eq. (14) is rewritten by splitting it into two components, one purely linear and another in which bi-linear forces are involved. Eq. (14) becomes

$$\mathbf{q}_{\mathrm{sys}.t} = \mathbf{q}_{\mathrm{sys.kn}} + \sum_{c}^{n_{\mathrm{cont}}} f_{\mathrm{cont}.c}\begin{pmatrix} \mathbf{u}_{\mathrm{c}}^{*c} \\ \mathbf{u}_{\mathrm{p}}^{*c} \end{pmatrix} + \sum_{d}^{n_{\mathrm{sd}}} f_{\mathrm{sd}.d}\begin{pmatrix} \mathbf{u}_{\mathrm{c}}^{*d} \\ \mathbf{0} \end{pmatrix}, \tag{15}$$

where n_{cont} and n_{sd} are the number of contact points and slackened droppers, respectively,

$$\mathbf{q}_{\mathrm{sys.kn}} = \mathbf{K}_{\mathrm{Int}}^{-1}\left[\mathbf{M}_{\mathrm{sys}}\hat{\ddot{\mathbf{q}}}_{t-\Delta t} + \mathbf{C}_{\mathrm{sys}}\hat{\dot{\mathbf{q}}}_{t-\Delta t} + \mathbf{f}_{\mathrm{sta.sys}}\right], \tag{16}$$

and those vectors denoted as $\mathbf{u}^*$ are the instantaneous linear responses of the system at positions where bi-linear forces, $f_{\mathrm{cont}.c}$ and $f_{\mathrm{sd}.d}$, are acting. The reduction of the computational cost provided by the method of Gregori et al. [37] relies on the fact that calculation of $\mathbf{u}^*$ is performed once during a pre-calculus stage. To solve Eq. (15), it is necessary to obtain the values of the forces

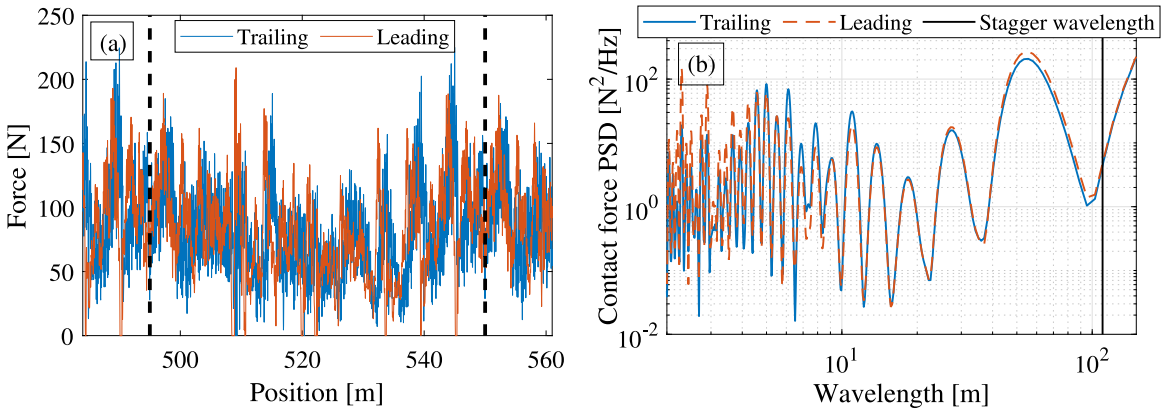

Fig. 4. (a): Unfiltered time-domain contact force results (Dashed black lines denote mast positions). Speed: 300 km/h. (b): Contact force PSD in the wavelength domain.

due to contact and those balancing the dropper slackening. Both are obtained after introducing the definition given in Eq. (15) into Eqs. (10) and (11), which results in a system of equations that is generally defined as

$$\begin{bmatrix} \mathbf{I}_{n_{\text{cont}}} - \mathbf{A} & \mathbf{B} \\ \mathbf{C} & \mathbf{I}_{n_{\text{sd}}} - \mathbf{D} \end{bmatrix} \begin{bmatrix} \mathbf{f}_{\text{cont}} \\ \mathbf{f}_{\text{sd}} \end{bmatrix} = \begin{bmatrix} \mathbf{E} \\ \mathbf{F} \end{bmatrix}. \tag{17}$$

The advantage of this procedure lies in the fact that convergence is performed over Eq. (17) instead of Eq. (13). The former has $n_{\text{cont}} + n_{\text{sd}}$ unknowns, whereas the latter involves all the system DoF. For a detailed explanation of the methodology, the reader is referred to the work of Gregori et al. [37]. Nevertheless, in Appendix A the definition of $\mathbf{u}^*$ in Eq. (15) and the terms in Eqs. (16) and (17), are presented as implemented here to consider multiple contact points, flexible contact strips and the Newmark integrator scheme. The correctness of the formulated mathematical model is confirmed by the standard EN-50318-2018 [15]. All the results are within the range given by this standard, and they are included in Appendix B.

3. The trace of the stagger in the pantograph accelerations

In this section, the OCL-pantograph interaction model defined above is used to determine whether the stagger has a noticeable influence on the system response. More specifically, the goal is to find a clear trace of the stagger on the vertical panhead accelerations. The panhead accelerations are predicted on contact strips at attachment points with the upper arm. The lateral displacement of the contact position oscillates with a frequency given by the ratio between the vehicle speed and the stagger wavelength; $V/2L_{\text{span}}$, hereinafter known as stagger frequency. For the span length used here, 55 m, this frequency lies between 0.25 Hz and 0.75 Hz for the speed range from 100 km/h to 300 km/h, respectively. Any dynamic effect caused by the stagger must be related to this frequency (or wavelength). Firstly, the dynamic response is analysed with conventional frequency analysis (Fourier analysis), and secondly, via time–frequency analysis (Wavelet analysis).

3.1. Conventional Fourier analysis

Contact forces, elastic forces at the strip attachment and strip accelerations are analysed in the time and frequency domains, the latter is made via the Power Spectral Density (PSD). For the sake of clarity, results are presented in terms of wavelength instead of frequency. Regarding contact forces, the results in Fig. 4(a) and (b) show the OCL-pantograph contact forces at the leading and trailing contact strips in the time (unfiltered) and frequency domains, respectively. The dynamic nature of contact forces is clear in Fig. 4(a). By studying the frequency-domain in Fig. 4(b), significant dynamic features are distinguished. They are caused by the pantograph and OCL dynamics and the characteristic lengths of the latter: span length and distance between droppers. However, at the stagger wavelength, there is no trace of a significant dynamic contribution.

Concerning the elastic forces at the strip attachment, Fig. 5(a) and (b) show forces due to the elastic part of the attachment elements at both sides of the leading strip, in time and frequency domains, respectively. In this case, the effect of the stagger is very noticeable. In the time-domain, the most significant dynamic feature coincides with the stagger wavelength in both forces. Moreover, this feature is out-of-phase in both signals. It occurs because each attachment element undergoes the highest compression when the contact wire approaches its location. Since the main contribution to the spring force is due to the stagger, it can be used to estimate the stagger, as done by Bocciolone et al. [5]. However, force measurements require invasive and/or expensive devices.

On the contrary to force measurements, acceleration ones have the advantage of being non-invasive and having a significantly lower cost. Fig. 6(a) and (b) show the time and frequency domains of the contact strip accelerations, respectively. The dynamic response of the acceleration is dominated by wavelengths below 10 m, which can be due to dropper spacing and flexible modes of the strips. Nevertheless, there is a significant dynamic response above 10 m. At 55 m, there is a peak due to the span length.

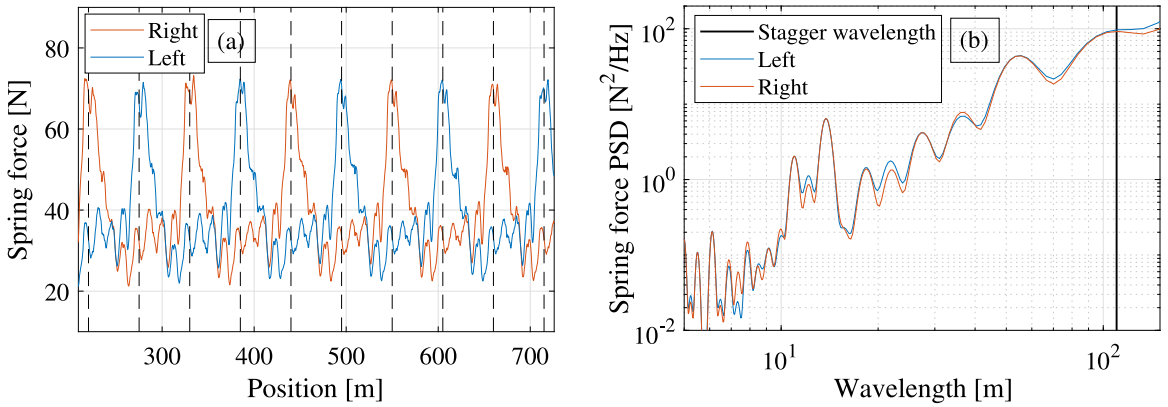

Fig. 5. Elastic component of the attachment forces at the leading strip. Speed: 300 km/h. (a): Unfiltered time-domain results (Dashed black lines denote mast positions). (b): PSD in the wavelength domain.

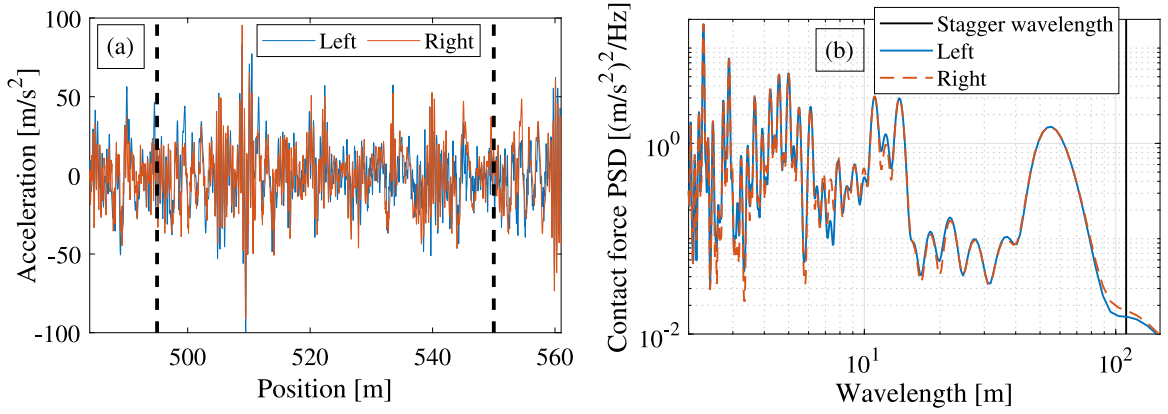

Fig. 6. Acceleration results for the leading contact strip at attachment positions. Speed: 300 km/h. (a): Unfiltered time-domain results (Dashed black lines denote mast positions). (b): PSD in the wavelength domain.

Moreover, noticeable responses are observed at 11 m and 13.7 m, which for 300 km/h corresponds to 7.5 Hz and 6.1 Hz. These frequencies are nearby the panhead solid vibration modes. However, at the stagger wavelength, there is an almost negligible signal content. This is the reason why using conventional Fourier analysis is unfeasible to estimate the OCL stagger.

3.2. Wavelet analysis

Time–frequency analysis is used here to find patterns in the acceleration signals that remain hidden through frequency analysis. The continuous wavelet transform (CWT) is chosen since it has a high level of resolution. Its definition reads

$$W(s,\tau) = \frac{1}{\sqrt{s}} \int_{-\infty}^{\infty} x(t)\, \psi^* \left(\frac{t-\tau}{s} \right) \mathrm{d}t, \tag{18}$$

where $x(t)$ is the analysed signal; $\psi(t)$ is a mother wavelet, * denotes the complex conjugate, τ is the location parameter related with time, and s is the dilation parameter related to frequency. In this work, the Morlet function is used as the mother wavelet.

Fig. 7(a) and (b) shows the scalogram of the wavelet power spectrum, $WP(s,\tau) = \left|W(s,\tau)^2\right|$, for the accelerations shown in Fig. 6(a). Due to the OCL periodicity, the wavelet power expresses periodic spatial behaviour in some frequency ranges. This spatial periodicity of the wavelet power is assessed by conventional Fourier analysis converting the spatial-domain into wavelength-domain. At each scale of the wavelet power, the spectral density is calculated as

$$\overline{WP}_j(\lambda) = \mathrm{PSD}\left[WP\left(s_j,\tau\right)\right], \tag{19}$$

where λ refers to wavelength. Fig. 7(c) and (d) show $\overline{WP}_j(\lambda)$ in which the space-domain in Fig. 7(a) and (b) is converted into wavelength-domain. The results in Fig. 7(c) and (d) confirm that the periodicity of the wavelet power is due to geometrical features of the OCL. The periodic behaviour is caused, on the one hand, by the span at its wavelength and first four upper harmonics, and on

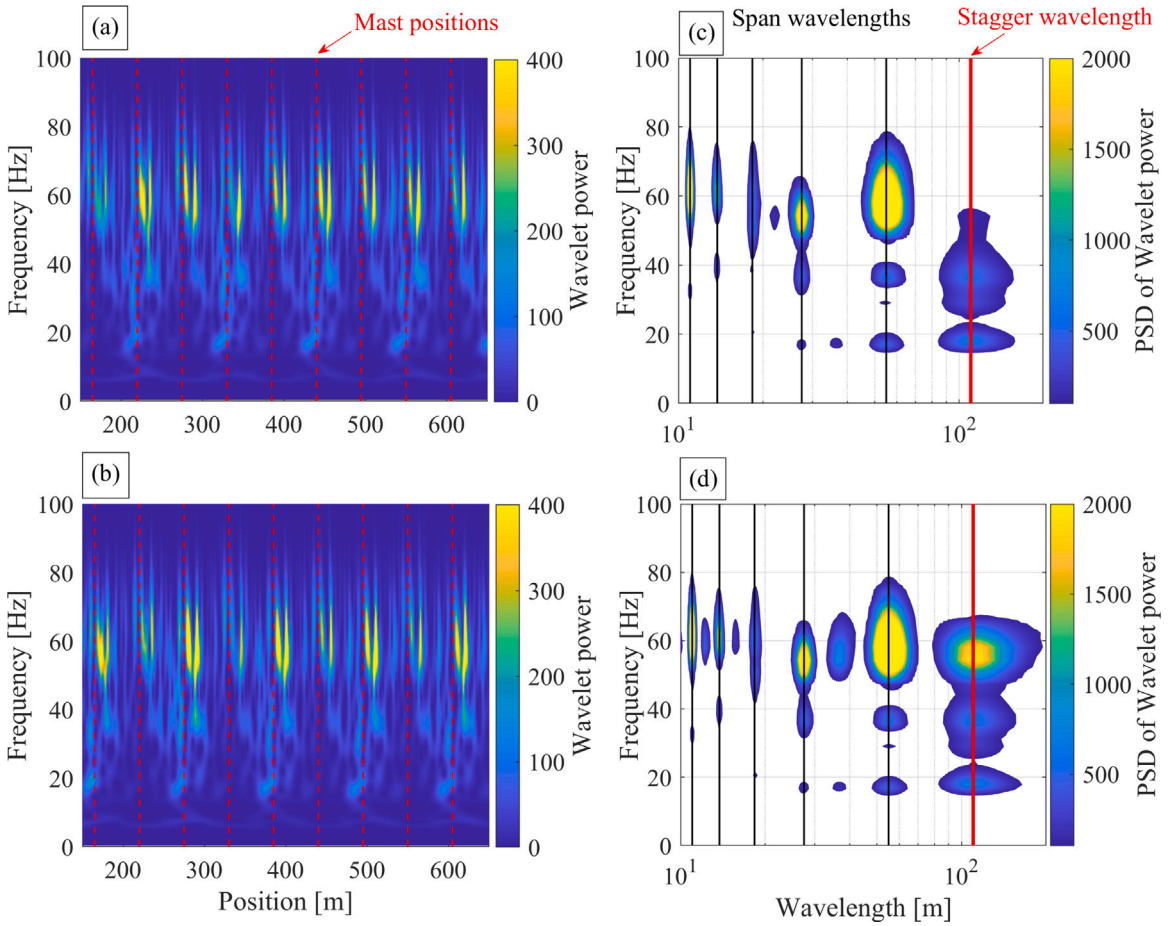

Fig. 7. Wavelet power of right (a) and left (b) accelerations of the leading contact strip and their Power Spectral Density representation (c) and (d), respectively.

the other hand, by the stagger wavelength. Whereas the former is dominant in periodicity of the dynamic behaviour above 50 Hz, the stagger wavelength causes a larger periodicity of the wavelet power below 50 Hz.

At this point, it is proved that the strength of the acceleration signals at strip attachment positions below 50 Hz is highly dominated by the stagger. Scale-averaged wavelet power (SAWP) can exploit this fact. It is defined as

$$\overline{W}^2(\tau) = \frac{\delta j \delta t}{C_\delta} \sum_{j=j_{\min}}^{j_{\max}} \frac{\left|W(s_j,\tau)\right|^2}{s_j}, \tag{20}$$

where C_δ is an empirically derived constant, δ_j and δ_t, are the scale and time steps [20]. The SAWP allows to examine fluctuations in power over a range of scales (from $j_{\min}$ to $j_{\max}$). The scales are set to capture the fluctuations between 5 Hz and 50 Hz.

Figs. 8(a) and (b) show the resulting SAWP for contact strip accelerations at both attachment positions. In both cases, the SAWP reaches a local maximum or minimum around the mast positions. As the contact wire shifts toward an accelerometer position, the related SAWP increases, whereas at the opposite accelerometer, the SAWP falls. Both Figs. 8(a) and (b) also display the raw SAWP as it is calculated at each time step and the averaged SAWP by using 5 m moving windows with 75 % of overlap. The use of moving windows has a reduced smoothing effect.

Finally, Fig. 8(c) shows Rt_{stag}, which combines SAWP of both accelerometers as

$$Rt_{\text{stag}} = \log_{10}\left(\frac{\text{SAWP}_{\text{right}}}{\text{SAWP}_{\text{left}}}\right). \tag{21}$$

The resulting processed signal has a pattern resembling the lateral position of the contact wire. In fact, it is almost directly proportional to the contact wire lateral position, but for some small perturbations. This strong relation between the CW lateral position and Rt_{stag}, makes the latter a powerful tool to define features for estimating the OCL stagger.

The OCL stagger can be non-centred in relation to the pantograph, which occurs during curve negotiation. Fig. 9(a) illustrates the range of lateral positions where pantograph-OCL contact occurs for centred and non-centred OCL stagger. Fig. 9(b) shows the

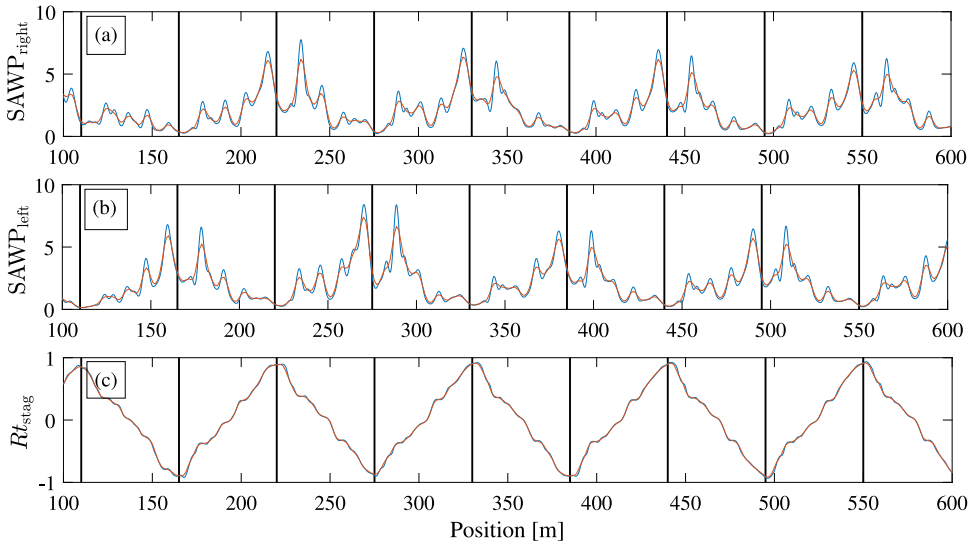

Fig. 8. SAWP from 5 to 50 Hz for the right (a) and left (b) positions of the leading contact strip. (c) Ratio between SAWP from (a) and (b), Rt_{stag}. Vertical black lines denote the mast positions. Blue: raw SAWP signal. Orange: averaged SAWP with moving window (5 m and 75 % overlap). (For interpretation of the references to colour in this figure legend, the reader is referred to the web version of this article.)

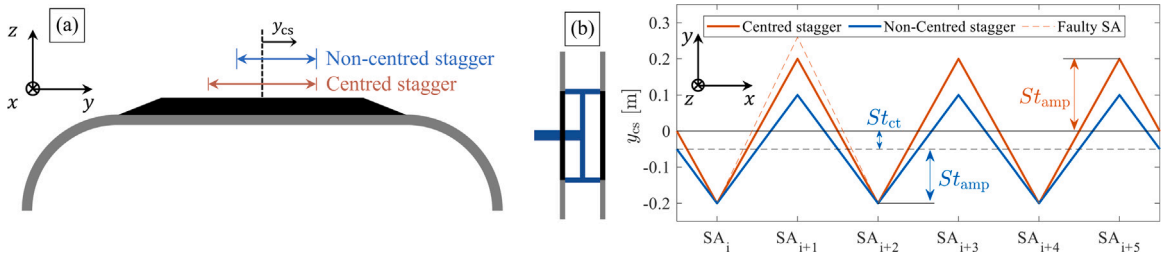

Fig. 9. (a) Frontal view of the pantograph with the range contact position due to centred and non-centred stagger. (b) Top view of the pantograph and the OCL line geometry for centred and non-centred stagger.

stagger amplitude, St_{amp}, and the stagger central position, St_{ct}. These values along with the distance between SAs (span length), are used to define the OCL lateral geometry. Fig. 9(b) also introduces the concept of faulty SA, which is used in Section 5.

The sensitivity of Rt_{stag} to the stagger is studied in Figs. 10(a) to (d), where the colour represents the range of simulated stagger amplitudes, St_{amp}, that encompasses from 0 m to 0.3 m. Figs. 10(a) and (b) address centred stagger, whereas in Figs. 10(c) and (d) non-centred stagger (St_{ct} = 0.1 m) is assessed. The results point out a proportional relation between St_{amp} and the amplitude of Rt_{stag}. This statement is further confirmed in Figs. 11(a) and (b), which shows the mean of the relative maximums and minimums in Rt_{stag} as a function of St_{amp} for the trailing and leading strips, respectively. Maximums occur when the CW approaches the sensor on the right side and vice versa. For centred situations, Figs. 11(a) and (b) show that the relation between the extreme values of Rt_{stag} and St_{amp} is almost linear. Moreover, mean values of the relative maximums and minimums are equal in magnitude.

As shown in Figs. 10(c) and (d), a non-centred stagger is also reflected by Rt_{stag}. Precisely, in its mean value, which is no longer zero. Another interesting feature lies in the magnitude of the extreme values with respect to the mean. When the stagger is shifted from the centre, since the CW moves closer to one of the measurement positions, the corresponding extreme values are more pronounced than those due to the opposite measurement position. Doubles arrows in Fig. 10(d) point out this phenomenon. Furthermore, non-centred stagger also affects the linearity between St_{amp} and the extreme values of Rt_{stag}. As shown in Figs. 11(a) and (b), the mean value of the minimums loses its linear relation with Rt_{stag} in non-centred case. Therefore, more complex relations arise between St_{amp} and Rt_{stag} as the CW gets close to the sensor position. Concerning both strips, the amplitude of Rt_{stag} is slightly higher on the trailing strip than in the leading one. Moreover, the extreme values of the leading strips are sharper, which might point out a better sensitivity to the stagger. Furthermore, for non-centred stagger situations, linear relation between St_{amp} and Rt_{stag} seems to be less distorted in the leading strip (Fig. 11(b)) than in trailing one (Fig. 11(a)).

3.3. The link between the OCL stagger and pantograph accelerations

The sensitivity of Rt_{stag} to the stagger is because when the CW approaches a measurement position, the measured acceleration-SAWP becomes maximum, whereas at the opposite measurement position it reaches its minimum value (Fig. 8(a) and (b)). As the

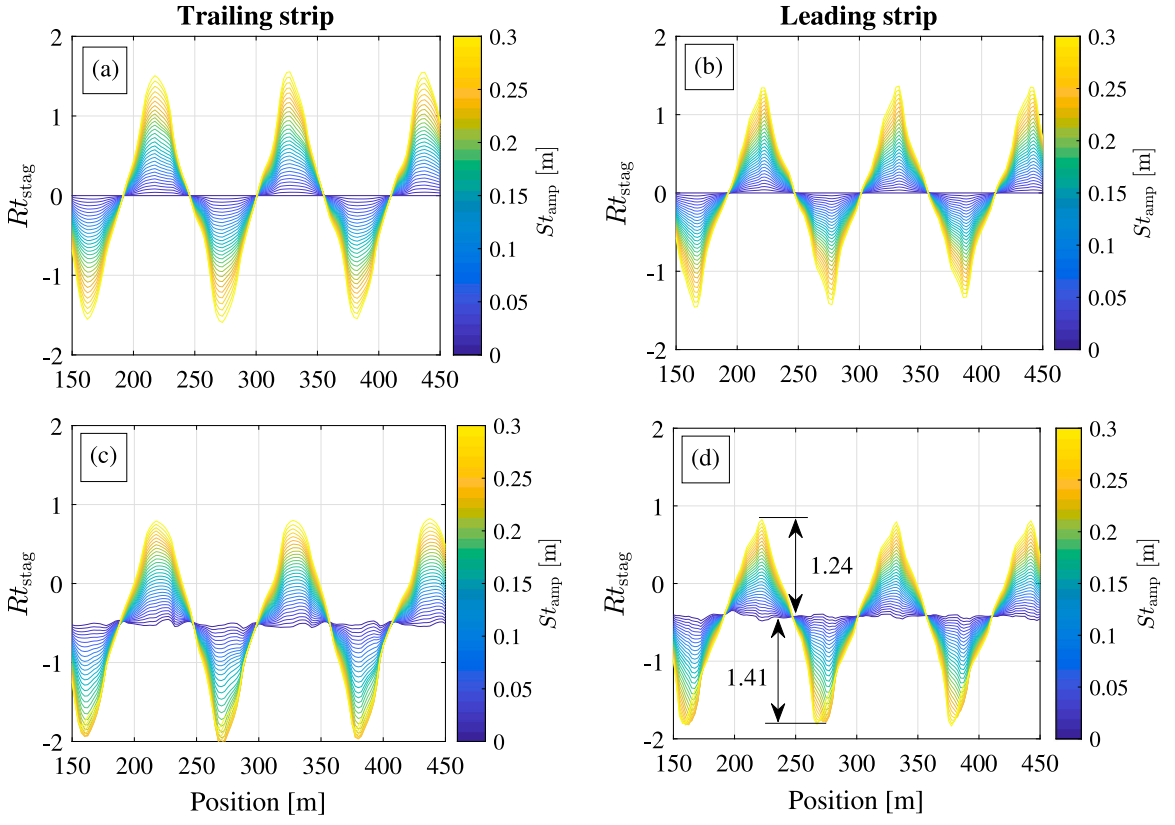

Fig. 10. Impact of the amplitude, st_{amp}, and offset, St_{ct}, of the stagger on Rt_{stag}. (a) and (b): centred stagger (St_{ct} = 0 m). (c) and (d): non-centred stagger (St_{ct} = −0.1 m). (For interpretation of the references to colour in this figure legend, the reader is referred to the web version of this article.)

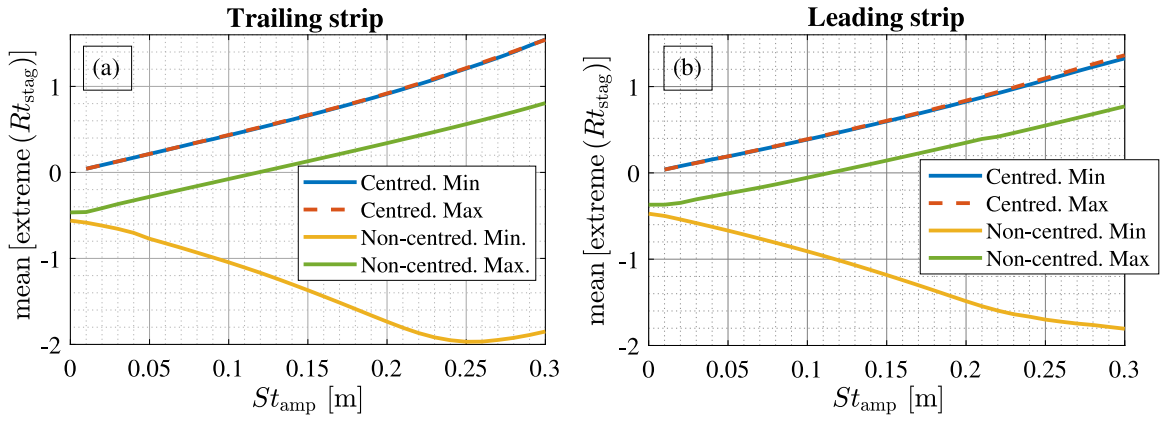

Fig. 11. Mean value of the relative maximums and minimums (extreme values) of Rt_{stag} as a function of the OCL stagger amplitude, St_{amp}. 'Centred. Min.' is plotted in absolute value to show the coincidence in magnitude with 'Centred. Max.'.

CW approaches a measurement position a constructive interference phenomenon arises, and on the opposite measurement position, destructive interference occurs. This phenomenon is qualitatively illustrated in Fig. 12(a), which depicts the motion of the contact strip when a force is applied eccentrically on it. The load eccentricity causes a moment load, which in turn involves contact strip rotation. At the closest measurement position, the displacement due to both rotational and translational motions add up, causing the mentioned constructive interference. However, at the opposite measurement position, these motions counter each other, resulting in destructive interference.

The phenomenon introduced above is confirmed by the calculated contact strip accelerances shown in Fig. 12(b). The accelerance is obtained at an attachment position (y_{cs} = 0.55 m) and the excitation takes place at the central position (y_{cs} = 0 m) and at

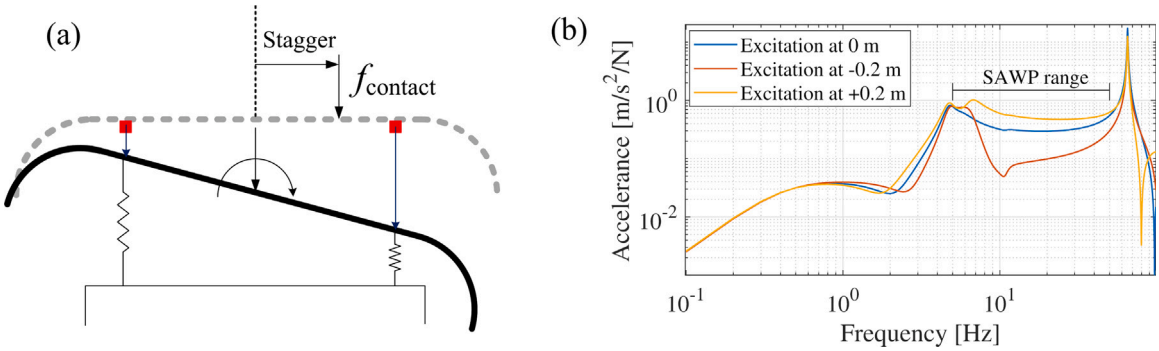

Fig. 12. (a) Scheme of the contact strip motion due to superposition of solid vibration modes with eccentric load (Sensor locations are denoted with red squares). (b) Accelerance of the contact strip at a measurement position for excitation at three different points.

$y_{cs} = \pm 0.2$ m. Statically and for low frequencies, there is no significant difference between accelerances due to the excitation position, since the response is dominated by the motion of the lower pantograph part. However, above the rigid vibration modes of the strips, about 5 Hz and 6.5 Hz for the translation and rotational motions, respectively, the system dynamics are controlled by inertia forces and the phenomenon pointed out in Fig. 12(a) becomes significant. As compared with excitation at $y_{cs} = 0$ m, when the loads shifts toward the sensor $(y_{cs} = 0.2\ \text{m})$, the accelerance increases. On the contrary, when the load moves away from the sensor, the accelerance largely decays. Above 50 Hz, flexible modes of the contact strips become dominant and the motion shown in Fig. 12(a) is no longer relevant. Fig. 12(b) also indicates the frequency range encompassed by SAWP. In this range, the accelerance is affected by the constructive and destructive interferences, which confirms the suitability of this choice.

4. Dependence of Rt_{stag} on pantograph features, speed and OCL uncertainties

In this section, the sensitivity of Rt_{stag} to different parameters is assessed. Firstly, the impact of pantograph features, specifically, the mass of the contact strips and the attachment stiffness. Secondly, the OCL geometric random deviation from its nominal configuration. And thirdly, the vehicle speed.

4.1. Impact of pantograph features on Rt_{stag}

Contact strip wear is an inherent consequence of the OCL-pantograph interaction, and therefore the reduction of the strip mass over the service life of the contact strip. This fact makes important the analysis of the mass influence on Rt_{stag}. A set of simulations is performed varying the height of the contact strip section corresponding to graphite. The change of mass is introduced homogeneously along the whole length of the graphite band. This assumption does not match the real behaviour of strip wear, which is concentrated mainly in the central part of the strip. Nevertheless, it allows checking the influence of the material loss on the Rt_{stag} qualitatively. The set of simulations encompasses heights of the graphite band from 2.5 cm to 1 cm, which involves a range of strip masses from 2.55 kg to 4.55 kg. The speed and stagger amplitude are set at 275 km/h and 0.2 m, respectively. The resulting Rt_{stag} is shown in Fig. 13(a) and (b), for the trailing and leading contact strips, respectively. The results indicate a large influence of the strip mass on Rt_{stag}, which mainly affects the amplitude of the response. The larger the contact strip mass is, the more sensitive Rt_{stag} becomes to St_{amp}. The shape of Rt_{stag} remains mostly unchanged for the leading strip, whereas it has a noticeable variation with mass for the trailing strip.

Concerning the strip attachment stiffness, its value is not expected to change significantly over the service life. Nevertheless, there might be some dispersion from one pantograph to another and therefore analysing its influence becomes of interest. Figs. 14(a) and (b) shows the impact of varying the stiffness of the springs in both contact strips. In this case, the influence is almost negligible for the leading strip and noticeable but still low for the trailing strip. Regarding the attachment damping, it is verified to influence Rt_{stag} even less than the attachment stiffness. This result is coherent with the spring-like nature of the attachment devices, which have an almost negligible damping ability at the low-frequency range.

The larger influence of the mass on Rt_{stag} is in agreement with its definition. The frequency range from which SAWP is obtained mainly encompasses the motion above the rigid vibration modes of the contact strips; consequently, SAWP is dominated by the strip inertia (Fig. 12(b)). The effect of the mass on Rt_{stag} is summarized in Fig. 15, which represents the evolution of the Rt_{stag} extreme values as function of the contact strip mass for different stiffness. The trends are similar in both leading and trailing strips, but the influence of the spring stiffness is almost negligible for the leading strip.

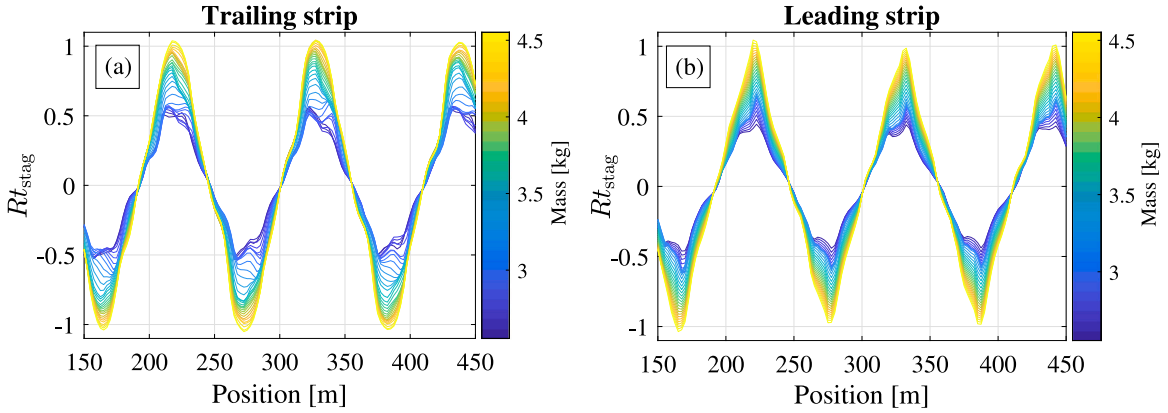

Fig. 13. Influence of the contact strip mass on the Rt_{stag}. (a) Trailing contact strip. (b) Leading contact strip. Speed set at 275 km/h. Stagger: 0.2 m. Spring stiffness: 1.75 kN/m.

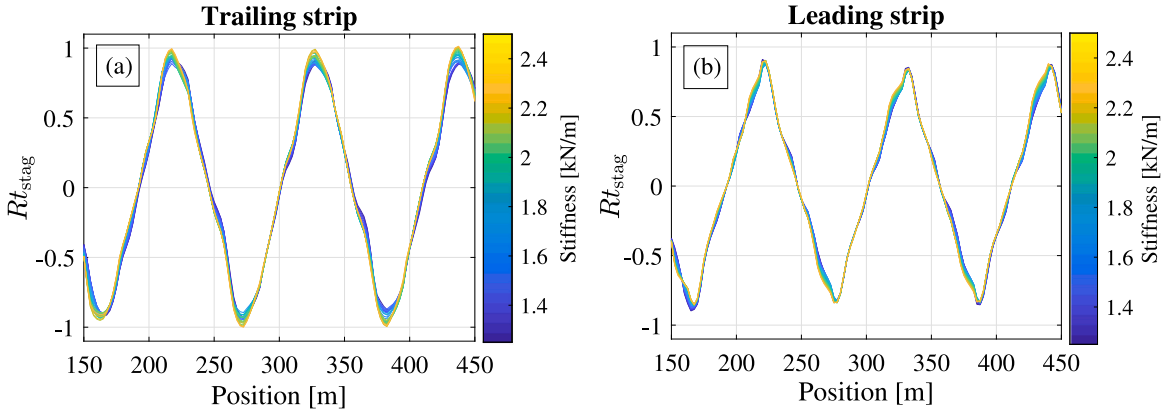

Fig. 14. Influence of the spring stiffness on the Rt_{stag}. (a) Trailing contact strip. (b) Leading contact strip. Speed set at 275 km/h. Stagger: 0.2 m. Strip mass: 3.89 kg.

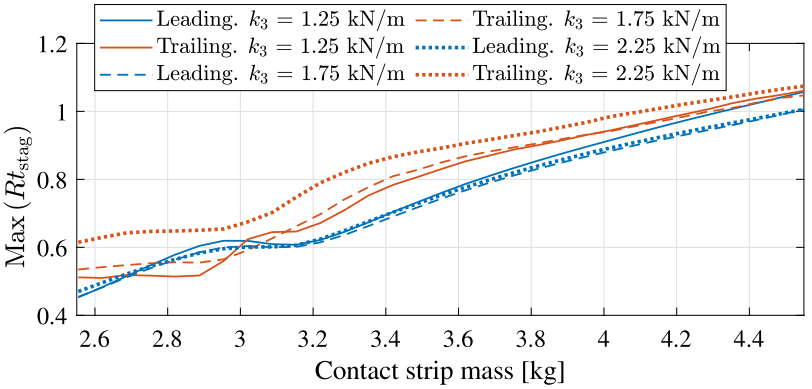

Fig. 15. Mean value of the relative maximum of $\left|Rt_{stag}\right|$ as function of the contact strip mass.

4.2. Impact of OCL geometry randomness on Rt_{stag}

As indicated in Section 2.2, in practice, the OCL installation undergoes departures from its nominal configuration. The randomness taken into account here is due to mast heights, dropper lengths, CW lateral position imposed by SAs, and CW wear. Excepting the last one, these uncertainties are introduced by defining standard deviations. Gregori et al. [35] use standard deviations of 6.6 mm and 2 cm for the dropper length and the mast height, respectively, which in turn are in accordance with experimental

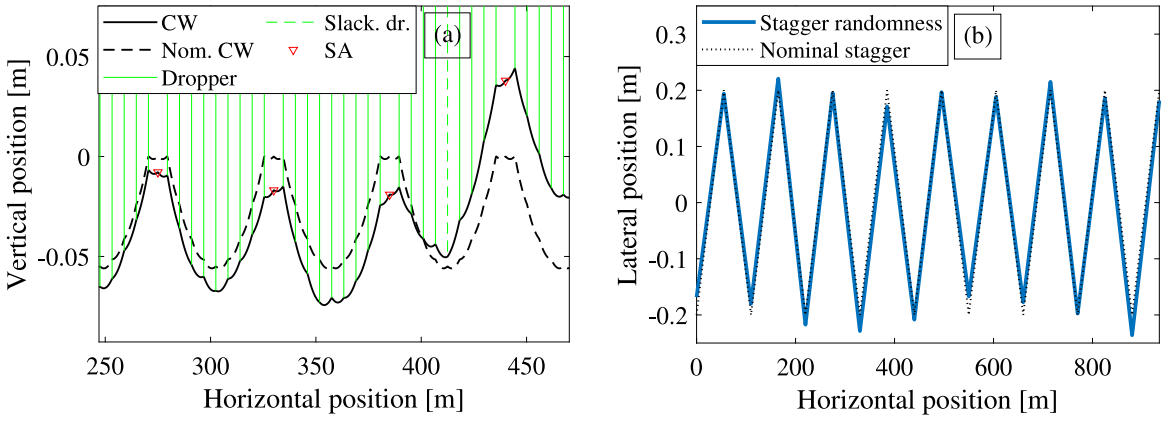

Fig. 16. (a): Vertical static position of the CW after introducing OCL randomness. (b): Stagger considering randomness in the lateral position imposed by SAs.

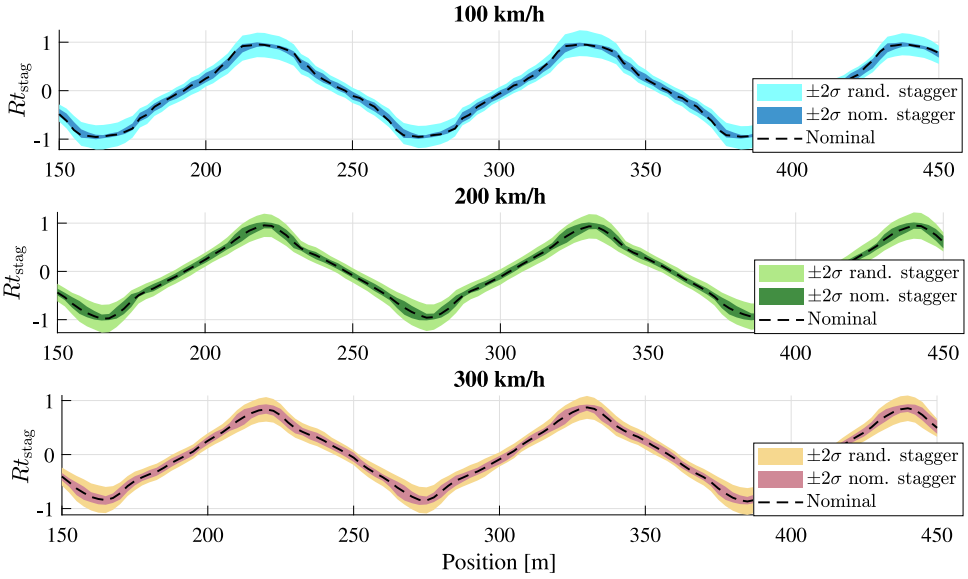

Fig. 17. Impact of geometrical randomness and CW wear on Rt_{stag} of the leading strip for different speeds.

measurements [38]. Fig. 16(a) shows the initial static position of the CW after including the mast height and dropper length randomnesses. The standard deviation of the lateral position imposed by the SA is set as a 10 % of the stagger amplitude. The resulting lateral CW position after introducing the latter randomness is shown in Fig. 16(b). Finally, the CW wear is introduced by using a PSD irregularity method. The PSD is taken from Collina et al. [16], and its amplitude is tuned to get wear levels not surpassing 3 mm.

Fig. 17 shows the impact of these randomnesses on Rt_{stag} of the leading strip for three different speeds. To assess the importance of stagger randomness, Fig. 17 also shows the dispersion if stagger keeps its nominal value whereas the other geometrical uncertainties are introduced. For each speed, one hundred simulations are performed for each case, with nominal and random stagger. The dashed line represents the nominal value (no randomness) of Rt_{stag}. Shade plots point out the dispersion of Rt_{stag} by encompassing two times its standard deviation. By comparing with the results neglecting stagger randomness, accounting for it significantly increases the overall dispersion of Rt_{stag}, and its influence tends to grow as the speed decreases. Around the mast position, the dispersion introduced by stagger randomness is the most noticeable, becoming clearly the dominant cause at 100 km/h. The results also denote a slightly lower scattering as the vehicle speed increases. Despite a certain degree of dispersion, Rt_{stag} seems a robust enough indicator to define features for the stagger estimation.

4.3. Impact of vehicle speed on Rt_{stag}

The influence of the speed on Rt_{stag} is assessed on Fig. 18. Fig. 18(a) depicts Rt_{stag} of the leading strip for several speeds from 40 km/h to 300 km/h. Both maximum values and shape of Rt_{stag} do not undergo significant variations due to the different

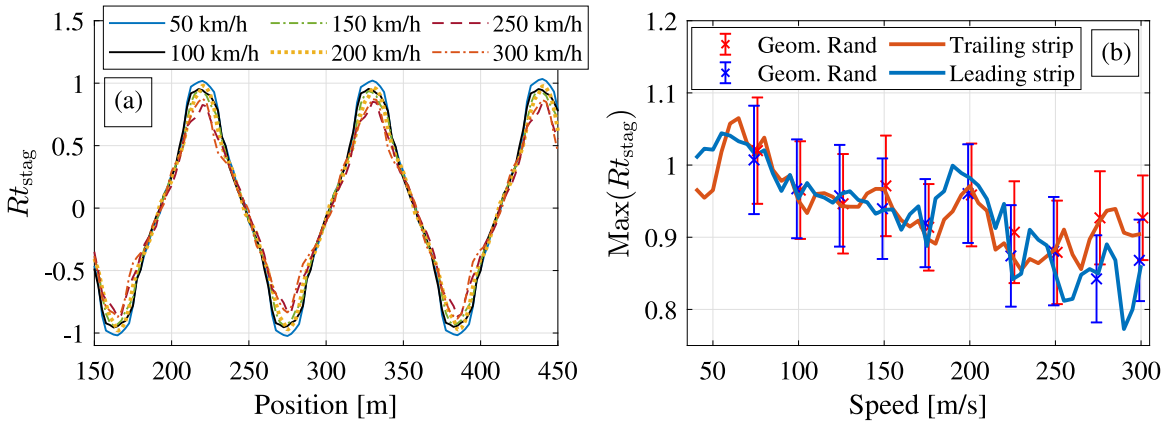

Fig. 18. (a) Rt_{stag} of the leading strip for different speeds. (b) Mean value of the relative maximums of Rt_{stag} as function of the vehicle speed (Solid line) and dispersion introduced by the geometrical randomness (The interval represents $\pm 2\sigma$). Stagger: 0.2 m. Strip mass: 3.89 kg. Spring stiffness: 1.75 kN/m.

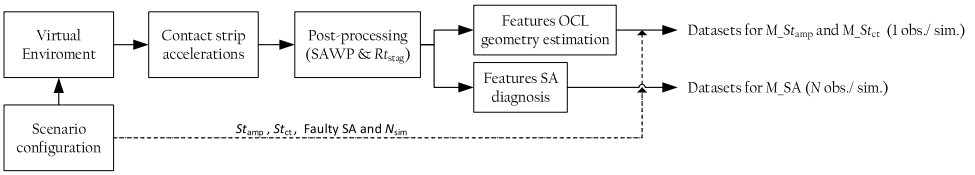

Fig. 19. Dataset generation process.

speeds. Therefore, the methodology is sensitive to stagger in the whole range of normal operation speeds. This fact is confirmed by Fig. 18(b), which shows the mean of the relative maximum in Rt_{stag} for both leading and trailing strips. The maximum values of Rt_{stag} tends to decrease as speed increases, from values of Rt_{stag} about 1.05 to 0.8 for 40 and 300 km/h, respectively. Fig. 18(b) also shows the dispersion introduced by the geometrical randomness. It is defined as in the previous sections and calculated from one hundred simulations at each speed. Each error bar encompasses $\pm 2\sigma\left(\mathrm{Max}\left(Rt_{stag}\right)\right)$. The uncertainty introduced by the geometrical randomness overlaps in a large extent the effect of the speed on $\mathrm{Max}\left(Rt_{stag}\right)$, and therefore it will tend to diminish its influence.

5. Model-driven machine learning for OCL geometry estimation and steady-arm diagnosis

This section proposes the use of machine learning (ML) models for the monitoring of the OCL by using panhead accelerations. More precisely, the acceleration of contact strips at their attachment positions. The definition and validation of the ML models rely on datasets generated by the virtual environment defined in Section 2. These datasets contain meaningful features of the contact strip accelerations formulated in terms of the signal processing presented in Section 3.

Three ML models are presented, M_St_{amp} and M_St_{ct}, which deal with the estimation of the OCL lateral geometry, and M_SA that addresses the detection of anomalous lateral CW position imposed by SAs. The outputs of M_St_{amp} and M_St_{ct} are St_{amp} and St_{ct}, respectively (Fig. 9(b)). The output of M_SA is a categorical value that determines whether a certain SA is healthy or faulty based on the lateral position that it imposes on the CW.

The rest of the section introduces, firstly, the description and definition of the training and validation datasets. The datasets description concerns the explanation of simulation scenarios, whereas the definition refers to the signal features building the datasets. Secondly, ML models for St_{amp}, St_{ct} and SA diagnosis are defined and validated.

5.1. Datasets description and generation

The dataset generation procedure is schematically shown in Fig. 19. It requires the definition of a set of scenarios to be simulated by the virtual environment. Each scenario establishes a certain number of simulations, N_{sim}. In turn, each simulation uses different values of St_{amp} and St_{ct}, as well as different numbers and positions for the faulty SAs. Subsequently, the simulated contact strip accelerations are post-processed to obtain their SAWP and Rt_{stag}, from which the ML models input features are defined. Once features are obtained, they are grouped together with the OCL geometry definition into observations. For the case of M_St_{amp} and M_St_{ct}, the features affect the whole OCL and therefore each simulation results in only observation. However, features used in M_SA are different since they concern individual SA positions, hence there will be as many observations as detected SA positions.

Table 2
Simulation scenarios description.

Scenario	Description	Objective	N_{sim}	Generated dataset
1	Feasible stagger	M_St_{amp} model generation M_St_{ct} model generation	600 (100 km/h) 600 (200 km/h) 600 (300 km/h)	Sc1_RD_{100} (600 obs.) Sc1_RD_{200} (600 obs.) Sc1_RD_{300} (600 obs.)
2	High disturbed SA	M_SA model generation	500 (100 km/h) 500 (200 km/h)500 (300 km/h)	Sc2_CD_{100} (5916 obs.) Sc2_CD_{200} (6052 obs.) Sc2_CD_{300} (5961 obs.)
3	Low disturbed SA	M_St_{amp} model individual performance analysis M_St_{ct} model individual performance analysis M_SA model individual performance analysis	200 (100 km/h) 200 (200 km/h) 200 (300 km/h)	Sc3_RPD_{100} (200 obs.) Sc3_RPD_{200} (200 obs.) Sc3_RPD_{300} (200 obs.) Sc3_CPD_{100} (2445 obs.) Sc3_CPD_{200} (2454 obs.) Sc3_CPD_{300} (2425 obs.)

Sc: Scenario, RD: Regressor Dataset, CD: Classifier Dataset, RPD: Regressor performance dataset, CPD: Classifier performance dataset.

5.1.1. Scenarios configuration

Three different scenarios are configured with complementary objectives (Table 2). Scenarios 1 and 2 are used to formulate ML models for the geometry estimation and the SA diagnosis, respectively. Scenario 3 represents intermediate situations between those of Scenarios 1 and 2, intending to check the performance of the ML models devoted to geometry estimation and SA diagnosis over the same data. For each scenario, batches of simulations are carried out for different mean values of V, 100 km/h, 200 km/h and 300 km/h. The speed at each simulation is randomly defined according to a normal probability distribution. It results in a standard deviation of 2.5 km/h around the indicated nominal speed. The scenarios introduce geometry randomness as defined in Section 4.2. Each simulation reproduces the dynamic interaction along 770 m, i.e. 14 spans. In total, the datasets include 3900 simulations of the OCL-pantograph dynamic interaction.

Scenario 1 encompasses feasible configurations of the CW lateral geometry. No faulty SAs are introduced. The resulting datasets, Sc1_RD_V, are employed for the training and cross-validation of the St_{amp} and St_{ct} ML models, M_St_{amp} and M_St_{ct}, respectively. Each simulation randomly picks a value of St_{ct}, between −15 cm to 15 cm. Following, St_{amp} is also randomly chosen in a range within $\pm\left(30-\left|St_{ct}\right|\right)$ cm. This definition limits the nominal CW lateral position to a range of ±30 cm in relation to the pantograph centre. In these datasets, each simulation provides one observation, which contains 2 target variables to be predicted. Three datasets are defined with 600 simulations, one for each speed aforementioned. In total, 1800 simulations are carried out.

Scenario 2 accounts for the presence of disturbed SAs, whose lateral positions are significantly modified to increase the population of faulty samples. The objective is to generate the datasets to train and cross-validate a model for SAs diagnosis, M_SA. In this case, each simulation contains three disturbed SAs out of a total of thirteen. As commented in Section 4.2, the lateral CW positions at SAs are simulated with a certain level of randomness around the design value. The disturbed SAs include an extra random displacement of ±5 cm on average and 2 cm of standard deviation. The classification is based on two categories, healthy or faulty SAs depending on whether their deviation over the nominal position is below or above 5 cm, healthy and faulty, respectively. This threshold defining faulty SAs is taken from Ngamkhanong et al. [39], which in turn obtain it from Australian OCL standards. The variables St_{amp} and St_{ct} defining nominal stagger are determined as in Scenario 1. Three datasets are generated corresponding to each speed, Sc2_CD_V, with 500 simulations per dataset. Each simulation obtains the response at thirteen SA positions per simulation, which means 6500 SA positions to assess. Due to the disturbed SAs and the inherent defined randomness, the faulty SAs represent around 11 % of each dataset.

Scenario 3 is similar to Scenario 2; however, it differs in that only one disturbed SA is introduced. This definition results to about 4 % of faulty SAs. The associated datasets, Sc3_RPD_V and Sc3_CPD_V, are used to observe the performance of the models trained in Scenarios 1 and 2 over the same data, respectively. For this purpose, 200 simulations have been carried out at each speed. It leads to six datasets. On the one hand, Sc3_RPD_V are involved in the validation of M_St_{amp} and M_St_{ct} with one observation per simulation. On the other hand, Sc3_CPD_V perform the validation of M_SA, with thirteen observations per simulation and therefore 2600 overtaken SA positions. In Table 2, the number of observations of the datasets involved in SA classification is slightly inferior to the number of SA positions overtaken in simulations. This difference is due to some of the SA positions are not detected in a step previous to its classification. This step is explained below in Section 5.1.3.

5.1.2. Datasets generation for the estimation of St_{amp} and St_{ct}

In Sc1_RD_V and Sc3_RPD_V, each observation contains an ensemble of features defined from the SAWP and Rt_{stag} results. A total of 36 features are considered potentially meaningful for the estimation of St_{amp} and St_{ct}. The features are equally defined at each contact strip, and therefore each one has 18 features. The feature description is included in Table 3. These features are the most common in the analysis of time and frequency domain signals. Most of these features can be obtained straightforwardly from SAWP and Rt_{stag} at a very low computational cost. However, some of them require a comment. Features 7 and 8 need the choice of a threshold to define what is taken as relative maximums and minimums. It is defined as a function of the peaks and notches prominence, and its value is set as 0.2.

Table 3
Features included in the datasets for the ML models (M_St_{amp} and M_St_{ct}).

Index	Feature	Description	Index	Feature	Description
1–2	mean (SAWP_i)	Mean value of SAWP for each ith sensor	3–4	std (SAWP_i)	Standard deviation of SAWP for each ith sensor
5	mean (Rt_{stag})	Mean value of Rt_{stag}	6	std (Rt_{stag})	Standard deviation of Rt_{stag}
7	mean $[\max(Rt_{stag})]$	Mean of the relative maximums of Rt_{stag}	8	mean $[\min(Rt_{stag})]$	Mean of the relative minimums of Rt_{stag}
9	Max (Rt_{stag})	Absolute maximum of Rt_{stag}	10	Min (Rt_{stag})	Absolute minimum of Rt_{stag}
11–14	WL $[\mathrm{PSD}(\mathrm{SAWP}_i)]_{1st,2nd}$	Wavelengths of the 1st and 2nd dominant peaks of the SAWP_i PSD for the ith sensor	15–18	$\lvert\mathrm{PSD}(\mathrm{SAWP}_i)\rvert_{1st,2nd}$	Magnitude of the 1st and 2nd dominant peaks of the SAWP_i PSD for the ith sensor

Table 4
Features included in the datasets for the ML model (M_SA).

Index	Feature	Description	Index	Feature	Description
1–2	$Rt_{stag.strip}$	Rt_{stag} at steady-arm position for both strips	3–6	$\mathrm{SAWP}_{sensor,strip}$	SAWP at steady-arm position for both strips and sensors
7	St_{amp}	OCL stagger amplitude	8	St_{ct}	OCL stagger central position

As mentioned in the previous section, the datasets for regressors are generated in both Scenario 1 and Scenario 3. In Scenario 1, for each of the speeds under study, 600 observations are generated with 36 features and two target variables. The target variables of M_St_{amp} and M_St_{ct}, which are St_{amp} and St_{ct}, respectively, maintain a uniform distribution, with possible values on [0, 0.3] m range for amplitude and [−0.07, 0.07] m for central position.

5.1.3. Datasets generation for the steady-arms diagnosis

In the datasets $\mathrm{Sc2\_CD}_V$, each observation corresponds to an individual SA position. Therefore, previous to the feature definition, it is necessary to determine SAs positions approximately. This pre-process exploits the fact that pronounced peaks and notches of Rt_{stag} are related to SAs (Fig. 8(c)). In order to label a peak or notch as a SA position, it is imposed that their prominence and width must be above 0.15 and 10 m, respectively. This minimum prominence is expected to detect most of the of SAs imposing stagger amplitudes above 0.05 m, which encompass those SAs at risk of causing dewirement. This claim is supported by results corresponding to centred stagger in Fig. 11, which show that maximum and minimum values of Rt_{stag} lower than 0.15 are due to stagger amplitudes below 0.05 m. Regarding the width of the peak, it simply acts as a high-pass filter of wavelengths about 10 m. With this threshold definition, about 7 % of the SAs positions are missed. However, false SA positions are avoided. Moreover, this procedure identifies about 99 % of the SAs positions corresponding to faulty ones. As it might be expected, most of the missed SAs occur for small values of St_{amp}, whose mean value is 2 cm with a standard deviation of 1 cm. This pre-process explains why the number of observations in $\mathrm{Sc2\_CD}_V$ (Table 2) is below the number of SA positions overtaken in simulations.

Once SA positions are located, the features are defined from SAWP and Rt_{stag} values at the corresponding locations. The description is included in Table 4. The values of St_{amp} and St_{ct} defined by the scenario configuration are also introduced as features. This fact involves that M_SA needs a previous knowledge of the OCL nominal geometry in order to perform the SA diagnosis. The target variable is categorical, it has two possible outcomes: healthy and faulty diagnosis.

5.2. Machine learning model generation and performance for steady-arms diagnosis

H2O AutoML is used to train and cross-validate the ML models: M_St_{amp}, M_St_{ct} and the M_SA [40]. It is an open-source, distributed, fast and scalable platform designed for the development of ML and predictive analytics. H2O AutoML works with the following types of models: deep learning models, gradient boosting machines, generalized linear models and distributed random forests. In addition, it makes use of the stacked ensemble technique to improve overall model accuracy [41].

For the analysis and training of the different models, a Docker container with R server has been deployed. The computer where the container is deployed has the following characteristics: Intel® Core™ i7-8700 CPU @ 3.2 GHz with 32 GB RAM. The resources allocated to Docker are 5 CPUs, 26.50 GB RAM and 1.5 GB of swap RAM.

5.2.1. Machine learning modelling for the estimation of stagger amplitude and central position

Following the guidelines defined at the beginning of this section, two batches of ML models are performed: M_St_{amp} and M_St_{ct}. In both batches, three models are trained, each one with the dataset corresponding to the speed to be analysed for estimation of St_{amp}: $M\_St_{amp\_100}$, $M\_St_{amp\_200}$ and $M\_St_{amp\_300}$; and for the estimation of St_c: $M\_St_{ct\_100}$, $M\_St_{ct\_200}$ and $M\_St_{ct\_300}$.

A total of 150 different ML models are trained for St_{amp} and St_{ct} and 100 models for the estimation of SA. In order to reduce the risk of overfitting, all training is performed with 10 folds in a cross-validation fashion. The dataset is divided into ten equal parts

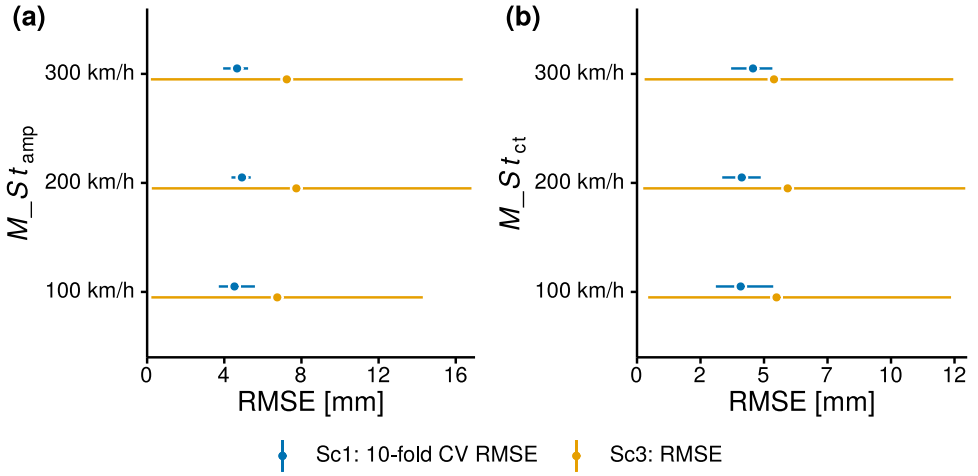

Fig. 20. (a): M_St_{amp} model RMSE (b): M_St_{ct} model RMSE. (For interpretation of the references to colour in this figure legend, the reader is referred to the web version of this article.)

in order to train with nine of them and validate with the tenth. Ten iterations are performed, changing the validation set. Through this methodology, the risk of overfitting can be reduced and a more reliable performance can be obtained.

The metric used for the valuation of the trained models M_St_{amp} and M_St_{ct} is the root-mean-square error (RMSE). This metric measures the amount of error between the observed values (v_i) and those predicted by the model $(\hat{v}_i)$. The RMSE is defined as

$$\text{RMSE} = \sqrt{\frac{1}{n}\sum_{i=1}^{n}(v_i - \hat{v}_i)^2}, \tag{22}$$

where n is the number of observations.

Fig. 20 shows the performance of the models M_St_{amp} and M_St_{ct}. The y-axis shows each speed under study. The x-axis shows the RMSE of the trained models: The blue colour shows the cross-validated results in Scenario 1, and the yellow colour shows the performance results of the models in Scenario 3, which includes one disturbed SA. The 95% confidence intervals (CI_{95}) show the performance uncertainty. The confidence intervals have been calculated using percentiles: the minimum corresponds to a percentile 2.5 and the maximum is the percentile 97.5.

The trained models show good performance for the estimation of St_{amp} and St_{ct}. The $M\_St_{amp\_100}$ model obtains a RMSE of 4.5 mm CI_{95} [3.7 mm, 5.5 mm], the $M\_St_{amp\_200}$ model obtains a RMSE of 4.9 mm CI_{95} [4.3 mm, 5.3 mm] and the $M\_St_{amp\_300}$ model has a RMSE of 4.6 mm CI_{95} [3.9 mm, 5.2 mm]. The $M\_St_{ct\_100}$ model obtains an RMSE of 4.0 mm CI_{95} [3.1 mm, 5.3 mm], the $M\_St_{ct\_200}$ model obtains a RMSE of 4.1 mm CI_{95} [3.3 mm, 4.8 mm] and $M\_St_{ct\_300}$ has an RMSE of 4.5 mm CI_{95} [3.7 mm, 5.3 mm].

On the other hand, the models trained in Scenario 1 have been evaluated for Scenario 3. The performance is shown in yellow colour. The RMSE value for St_{amp} and St_{ct} lies around 7.2 mm CI_{95} [0.21 mm, 15.8 mm] and 5.6 mm CI_{95} [0.32 mm, 12.5 mm], respectively.

The confidence intervals for Scenario 1 and Scenario 3 overlap, which discards the risk of overfitting. The results show differences between those obtained for Scenario 1 and Scenario 3. These differences are reasonable because the ML models are trained with Scenario 1, whereas datasets from Scenario 3 are unknown by them. Therefore, the prediction in the case of Scenario 3 results in larger RMSE and wider confidence interval than in Scenario 1. Nevertheless, these errors levels are considered still acceptable.

Overall, the results indicate that the proposed methodology can be used for monitoring the health status of the stagger amplitude and its RMSE is independent of the speed.

5.2.2. Machine learning modelling for diagnosis of steady-arms

Three classification models are trained, one for each speed studied. The method followed for the training of these models is identical to that followed for the training of M_St_{amp} and M_St_{ct} models. The H2O AutoML library is used again. For each of the three speeds, 100 models are trained, keeping the 10 fold cross-validation to prevent overfitting.

As mentioned in the scenario configuration, only 11 % of cases are faulty SA in Scenario 2 and 4 % in Scenario 3. This is a case of an imbalanced classification problem. For this reason, the AUC-PR Curve (Area Under the Precision–Recall Curve) metric is taken into account [42]. Both precision and recall are focused on predicting the minority class (the faulty cases). Their definitions read

$$\text{Precision} = \frac{\text{TP}}{\text{TP} + \text{FP}}, \tag{23}$$

$$\text{Recall} = \frac{\text{TP}}{\text{TP} + \text{FN}}, \tag{24}$$

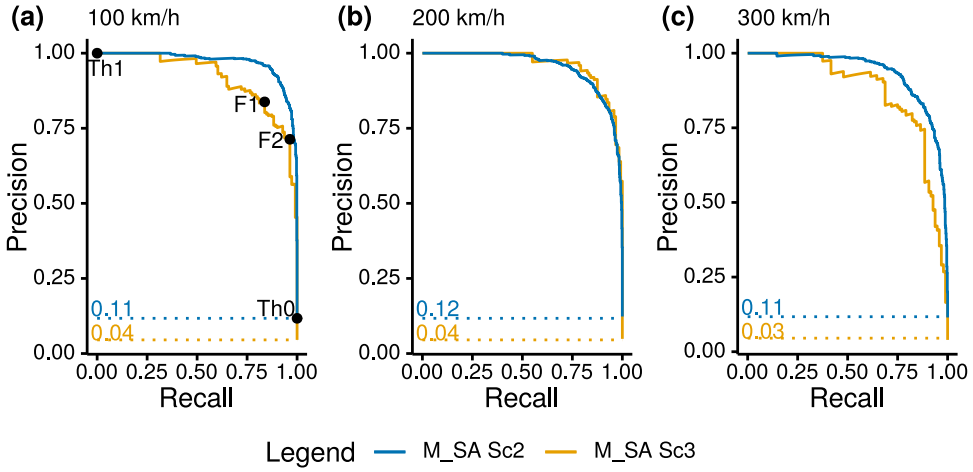

Fig. 21. *M*_SA PR-curve on Scenario 2 and Scenario 3. (For interpretation of the references to colour in this figure legend, the reader is referred to the web version of this article.)

where TP is a count of true positive of faulty cases, FP is a count of false positive of faulty cases and FN is a count of false negative of faulty cases. Precision is a metric that quantifies the number of correct positive predictions made. The result is a value between 0 and 1, where 0 refers to no precision and 1 to full or perfect precision. Recall is a metric that quantifies the number of correct positive predictions made out of all positive predictions that could have been made. Like Precision, the result is a value between 0 and 1. The baseline value is calculated for comparison purposes. Baseline is defined as

$$\text{Baseline} = \frac{N_{\text{Positive}}}{N_{\text{Observations}}}, \tag{25}$$

where N_{Positive} and $N_{\text{Observations}}$ are the number of positive cases and the number of observations, respectively. If all predictions were faulty for the SA diagnosis, it would be the case of having 0 false negatives. Consequently, the precision would be equal to the baseline, since TP + FP would equal the number of observations.

Fig. 21 shows the PR curve results of the *M*_SA (blue line) in Scenario 2 and *M*_SA (yellow line) in Scenario 3. The dotted line refers to the baseline value. The PR curve is plotted with Precision on the y-axis and Recall on the x-axis.

During diagnosis, the model *M*_SA assigns a certain probability to each observation. If the probability is higher than a chosen threshold, the observation is flagged as a faulty diagnostic, if it is less, the classification is healthy. All possible values of Precision and Recall depend on the chosen probability threshold. The values of this threshold range from 0 to 1:

- If the threshold is set to 0 (Th_0):
  - All observations are flagged as a positive class (faulty condition).
  - It would be the case to have 0 FN, so Recall takes the value of 1.
  - TP + FP would be equal to the number of observations, so Precision takes the value of the baseline.
  - This configuration is represented in the graph by the point of intersection between the dotted line and the continuous curve (Precision_{Th0}, Recall_{Th0}) = (Baseline, 1) (See Fig. 21(a)).
- If the threshold is set to 1 (Th_1):
  - All observations are flagged as the negative class (healthy condition).
  - TP is 0. Thus, Recall takes the value of 0
  - TP and FP take the same minimum, so Precision takes the value of 1.
  - This configuration is represented on the graph by the leftmost point of the curve (Precision_{Th1}, Recall_{Th1}) = (1, 0) (See Fig. 21(a)).
- In each of the models, the curve is given by shifting the probability threshold from 0 to 1. The curve has as many midpoints as dataset observations.

The decision as to which threshold to choose is in the hands of the user-defined strategies. Usually, for the selection of this threshold, F-measure (F-score) is used. The threshold is defined to make maximum the value of F-measure. There are several ways to obtain this value. One of them is F_1, which is defined as

$$F_1 = \frac{TP}{TP + \frac{1}{2}(FP + FN)}. \tag{26}$$

Table 5
*M*_SA AUC-PR on Scenario 2 and Scenario 3.

Model	100 km/h			200 km/h			300 km/h		
	Baseline	AUC-PR	CI_{95}	Baseline	AUC-PR	CI_{95}	Baseline	AUC-PR	CI_{95}
*M*_SA Sc2	0.11	0.970	[0.961, 0.978]	0.12	0.952	[0.942, 0.962]	0.11	0.934	[0.919, 0.947]
*M*_SA Sc3	0.04	0.918	[0.875, 0.952]	0.04	0.960	[0.935, 0.979]	0.03	0.872	[0.813, 0.922]

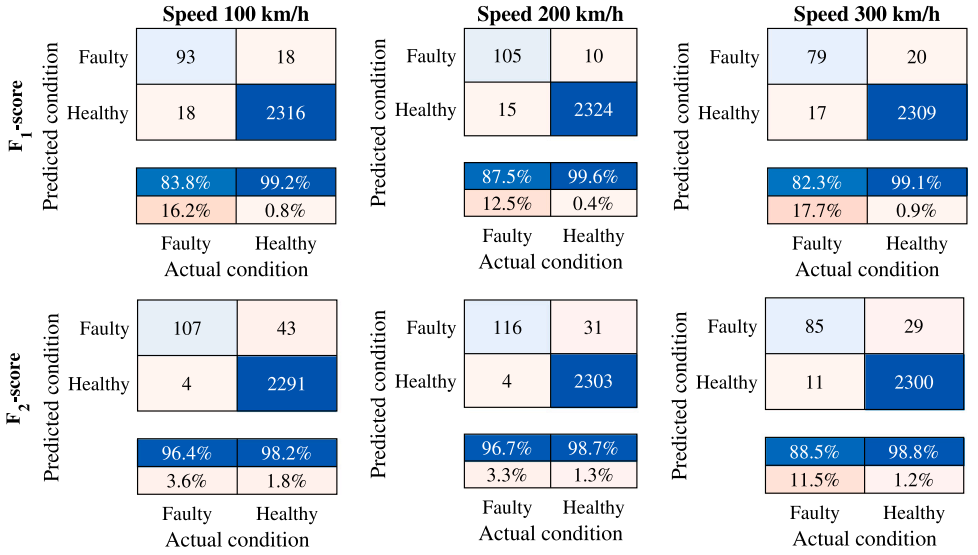

Fig. 22. Confusion matrices of the resulting diagnosis performed by *M*_SA over Scenario 3. The probability threshold is set according to F_1-score and F_2-score.

In this case, the measure gives equal weight to false negatives and false positives. Considering that the applicability of the proposed strategy is for the diagnosis of SA, it may affect more the occurrence of false negative cases (A faulty case that the *M*_SA diagnoses as healthy). Therefore, other metrics have been evaluated for the definition of the threshold. For example, the F_2 measure that gives more weight to recall than to precision and is defined as

$$F_2 = \frac{5TP}{5TP + 4FP + FN}. \tag{27}$$

Fig. 21(a) shows the points on the PR curve related to those thresholds that make maximum F_1 and F_2, whose values are 0.59 and 0.10, respectively.

Table 5 shows the AUC-PR results of the three trained *M*_SA models on Scenario 2 compared to results of the models on Scenario 3. All models show very good performance in terms of AUC-PR. The possible range of values for the AUC-PR is between baseline and 1, where baseline is the worst value and 1 is the best. In both scenarios, the value is closer to 1. The results are worse in Scenario 3 because the models have been trained for Scenario 1. This is also the reason for the increase in confidence intervals. No relationship is observed between train velocity and models' performance. The results show a significant difference between the PR curve with its respective baseline for each of the speeds analysed. The performance decreases in Scenario 3 because the models have been trained for Scenario 1.

The diagnoses performed by *M*_SA are shown in Fig. 22 by using confusion matrices. These results are obtained using the probability thresholds that make maximize F_1 and F_2. These matrices represent the TP and TN in the diagonal boxes, whereas FN and FP are introduced in the bottom-left and upper-right boxes, respectively. Below each confusion matrix, a table shows relative values, where the first and second rows represent the percentages of true and false diagnoses, respectively, for faulty and healthy SAs. It is observed that *M*_SA using the F_1 threshold can detect between 80 and 90% of the faulty SA positions, whereas more than 99% of the healthy SAs are correctly classified. To avoid missing faulty SAs, that is reducing FN, the threshold obtained accordingly to F_2 might be used. In this case, about 96% of the faulty SAs are detected at 100 and 200 km/h, whereas 88.5% are detected at 300 km/h. This improved detection of faulty SA is achieved at the cost of increasing the number of healthy SA positions diagnosed as faulty (FP).

6. Discussion

At present, the measurement of the OCL stagger with instrumented vehicles is based on force sensors and vision systems. Until now, inertial measurements had not been considered to perform this task. This barrier arises from the low value of the stagger

frequency, below 1 Hz. However, the theoretical work developed here shows the potential of contact strips accelerations to monitor the OCL stagger.

The methodology presented here proposes a new monitoring capacity of inertial measurements obtained in pantograph panhead. Therefore, it fosters the use of cheaper and less invasive monitoring strategies for the railway infrastructure. The methodology is based on a clear connection between the OCL stagger and the vertical panhead accelerations that this work establishes.

The analysis of the simulated pantograph signals revealed that the contact strips motion within a particular frequency range and at side positions has periodic patterns dominated by the stagger frequency. The proposed time–frequency signal processing based on the CWT and SAWP exploits this behaviour. The resulting output is Rt_{stag}, a time-domain non-dimensional value with a highly linear relation with the stagger.

To assess the method reliability, this work studies the sensitivity of Rt_{stag} to diverse sources of randomness. This analysis confirms that Rt_{stag} is robust to geometric uncertainties of the OCL, vehicle speed and stiffness of the attachment elements. However, the contact strip mass has a significant impact on Rt_{stag}, changing the sensitivity of Rt_{stag} to the stagger amplitude as the contact strip mass varies. Besides that, there are no significant differences between Rt_{stag} predicted on the leading and trailing contact strips, which might ease the implementation since only one instrumented contact strip could monitor stagger in both travel directions.

The use of a virtual environment has allowed the training of model-driven ML models to identify undesired and uncommon situations such as the ones addressed here, the faulty steady-arms. This is a key point of the proposed methodology as compared with analogous data-driven ML models, in which the lack of labelled data associated with extreme circumstances would hinder its formulation. Nevertheless, the final assessment of the methodology must be addressed with real measurements. It is also worth highlighting the contribution in the railway sector made by demonstrating the advantages of tools such as AutoML in their usefulness to visualize the estimation possibilities more accurately and efficiently.

In this work, the features employed for the training of the ML models are those most common in the analysis of both time and frequency domain signals. Nevertheless, a sensitivity analysis of ML models to these features would increase the understanding of the methodology. Subsequently, it may lead to consider some features not relevant for the ML models and to enhance them by using specific new features.

Before considering a fully operational implementation of the methodology two main issues should be addressed. Firstly, the reduction during the service life of the contact strip mass due to wear. Despite this could involve some challenges for a monitoring strategy based on this methodology, it opens the door to monitor together both stagger and contact strip wear. Secondly, the monitoring under varying speed conditions. On the one hand, it does not involve significant changes from the point of view of the signal analysis, as long as signals are transformed from the time to the spatial domain once wavelet transformation is performed. Nevertheless, this task would require a positioning system. On the other hand, varying speed conditions may affect the value of the features inputted to the ML models. If the speed variation is smooth enough, the current method might be still valid since the influence of speed on Rt_{stag} is not dominant. Furthermore, the ML models are trained with simulations performed at different constant speeds randomly chosen within a certain range. Moreover, geometrical randomness tends to fade even more the influence of the speed. Nevertheless, the applicability of ML models trained under constant speed condition to varying speed situations is a subject of further detailed study. Another alternative is creating datasets under non-constant speed conditions, but it would increase significantly the number of feasible scenarios to be simulated.

7. Conclusions

The presented methodology shows the potential of predicting the lateral OCL geometry and detecting faulty steady-arms by using inertial measurements of the panhead. The main conclusions of this work are following stated:

(a) The dynamic response of the pantograph contact strips is significantly affected by the change of the lateral contact position due to the stagger.
(b) The influence of the stagger is highly noticeable in the contact strip accelerations at side positions. The frequency range of interest is limited by the first rigid and flexible vibration modes of the contact strips, about 5 Hz and 50 Hz for the pantograph model used here.
(c) Non-centred loads on the pantograph due to the stagger cause alternate constructive and destructive interference on contact strip motion at side positions. The methodology relies on this phenomenon to monitor the stagger.
(d) Via time–frequency analysis of the signals, more specifically the Scaled Average Wavelet Power, meaningful features to monitor the lateral OCL geometry are obtained. The proposed signal analysis is robust to geometrical uncertainties, and it is valid in a wide range of vehicle speeds. However, it is highly affected by the mass change of the contact strips.
(e) The ML models show a good performance for low, medium and high speeds. Regarding geometry estimation, the stagger amplitude and the stagger central positions are predicted with an RMSE of approximately (4.7 ± 1.0) mm and 4.2 mm on average, respectively. Concerning the diagnosis of steady-arms, the ML models have an average predictive capability of 95 AUC-PR to assess whether a steady-arm is healthy or faulty.
(f) The performance of both ML model types is further observed by using them over a common dataset with a different configuration to that of the training datasets. In this case, the estimation of amplitude and central position have RMSE of 7 mm and 5.6 mm, respectively; whereas the ability to perform a correct classification is around 0.90 AUC-PR. The latter translates into detection rates of the faulty steady-arms about 96% at 100 and 200 km/h, and around 88% at 300 km/h.

Table 6
Static validation of the simple AC OCL model (EN-50318-2018 [15]). Dropper length error must be below 10 mm. Elasticity error must be below ±0.1 mm/N.

Dropper no.	Dropper length			Elasticity		
	Standard [mm]	Model [mm]	Error [mm]	Standard [mm/N]	Model [mm/N]	Error [mm/N]
Sup.	–	–	–	0.206	0.196	−0.010
1	1023	1027	4	0.165	0.166	0.001
2	902	908	6	0.273	0.266	−0.007
3	815	822	7	0.345	0.338	−0.007
4	764	771	7	0.388	0.381	0.007
5	747	754	7	0.400	0.396	0.004

Table 7
Dynamic validation of the simple AC-OCL model (obtained values and acceptance ranges).

Speed [km/h]	275				320			
Pantograph	Leading		Trailing		Leading		Trailing	
	Result	Range	Result	Range	Result	Range	Result	Range
Mean force [N]	144	[141.5, 146.5]	143	[141.5, 146.5]	167	[166.5, 171.5]	168	[166.5, 171.5]
σ [N]	32.7	[31.9, 34.8]	54.1	[50.0, 54.5]	52.1	[49.5, 62.9]	36.3	[30.2, 43.8]
$\sigma_{0\text{–}5\ \mathrm{Hz}}$ [N]	26.5	[26.4, 28.9]	45.1	[41.2, 45.4]	41.5	[38.7, 44.4]	17.6	[14.3, 23.3]
$\sigma_{5\text{–}20\ \mathrm{Hz}}$ [N]	19.0	[16.2, 22.4]	30.8	[25.2, 34.7]	31.5	[29.0, 46.2]	34.4	[26.7, 38.2]
Max. force [N]	237	[219, 244]	277	[241, 290]	301	[295, 343]	269	[252, 317]
Min. force [N]	86	[71, 86]	23	[14, 50]	66	[55, 82]	47	[21, 86]
Vert. position range [mm]	45	[19, 49]	61	[53, 70]	50	[39, 51]	24	[18, 35]
Max. uplift [mm]	43	[39, 48]	46	[45, 54]	60	[57, 64]	55	[50, 61]

Declaration of competing interest

The authors declare that they have no known competing financial interests or personal relationships that could have appeared to influence the work reported in this paper.

Funding

This project has received funding from the European Union's Horizon 2020 research and innovation programme and from the European Union Agency for the Space Program (EUSPA) under grant agreement No. 776402.

Appendix A. Terms for the dynamic OCL-pantograph interaction.

According to the Newmark's method, the variables in Eq. (14) are defined as

$$\mathbf{K}_{\mathrm{Int}} = \frac{1}{\beta \Delta t^2}\mathbf{M}_{\mathrm{sys}} + \frac{\gamma}{\beta \Delta t}\mathbf{C}_{\mathrm{sys}} + \mathbf{K}_{\mathrm{sys}}, \tag{A.1}$$

$$\hat{\mathbf{q}} \equiv -\left[\frac{\gamma}{\beta \Delta t}\mathbf{q}_{\mathrm{sys}.k} + \left(\frac{\gamma}{\beta} - 1\right)\dot{\mathbf{q}}_{\mathrm{sys}.k} + \left(\frac{\gamma}{2\beta} - 1\right)\Delta t \ddot{\mathbf{q}}_{\mathrm{sys}.k}\right], \tag{A.2}$$

$$\hat{\hat{\mathbf{q}}} \equiv -\left[\frac{\gamma}{\beta \Delta t^2}\mathbf{q}_{\mathrm{sys}.k} + \frac{1}{\beta \Delta t}\dot{\mathbf{q}}_{\mathrm{sys}.k} + \left(\frac{1}{2\beta} - 1\right)\ddot{\mathbf{q}}_{\mathrm{sys}.k}\right], \tag{A.3}$$

where γ and β are parameters of the integrator set in 0.5 and 0.25, respectively, which results in the average acceleration method. The instantaneous response vectors in Eq. (15) read

$$\mathbf{u}_{\mathrm{c}}^{*c} = \sum_{i \in \mathrm{DoF}_{\mathrm{c}}^{c}} \mathbf{K}_{\mathrm{int}}^{-1}\mathbf{B}_{\mathrm{c}.i} N_{\mathrm{c}.i}\left(x_c\right), \tag{A.4}$$

$$\mathbf{u}_{\mathrm{p}}^{*c} = \sum_{i \in \mathrm{DoF}_{\mathrm{p}}^{c}} \mathbf{K}_{\mathrm{int}}^{-1}\mathbf{B}_{\mathrm{p}.i} N_{\mathrm{p}.i}\left(y_c\right), \tag{A.5}$$

$$\mathbf{u}_{\mathrm{c}}^{*d} = \mathbf{K}_{\mathrm{int}}^{-1}\mathbf{B}_{\mathrm{c}.d}, \tag{A.6}$$

where $\mathrm{DoF}_{\mathrm{c}}^{c}$ and $\mathrm{DoF}_{\mathrm{p}}^{c}$ refer to the OCL and pantograph DoF involved in the cth contact position, respectively. The terms $\mathbf{B}_{\mathrm{c}.i}$ and $\mathbf{B}_{\mathrm{c}.d}$ are both Boolean vectors, the former has unitary values at the ith DoF, and the latter has non-zero values for the DoF at both

ends of the slackened droppers, 1 and −1 for the contact and messenger wires. The terms $N_{\mathrm{c}.i}(x_c)$ and $N_{\mathrm{p}.i}\left(y_c\right)$ represent the value of the OCL and pantograph shape functions, respectively, associated to the ith DoF at the longitudinal and lateral coordinates of the cth contact position, x_c and y_c, respectively.

The terms of the vector and matrices in Eq. (17) are defined as

$$A_{c_i,c_j} = -k_{\mathrm{cont}}\mathbf{N}_{c_i}\begin{pmatrix}\mathbf{u}_{\mathrm{c}}^{*c_j}\\ \mathbf{u}_{\mathrm{p}}^{*c_j}\end{pmatrix} \quad , \quad B_{c_i,d_j} = -k_{\mathrm{cont}}\mathbf{N}_{c_i}\begin{pmatrix}\mathbf{u}_{\mathrm{c}}^{*d_j}\\ \mathbf{0}\end{pmatrix}, \tag{A.7}$$

$$C_{d_i,c_j} = -\mathbf{k}_{\mathrm{d}.d_i}\mathbf{n}_{\mathrm{d}.d_i}\begin{pmatrix}\mathbf{u}_{\mathrm{c}}^{*c_j}\\ \mathbf{u}_{\mathrm{p}}^{*c_j}\end{pmatrix} \quad , \quad D_{d_i,d_j} = -\mathbf{k}_{\mathrm{d}.d_i}\mathbf{n}_{\mathrm{d}.d_i}\begin{pmatrix}\mathbf{u}_{\mathrm{c}}^{*d_j}\\ \mathbf{0}\end{pmatrix}, \tag{A.8}$$

$$E_{c_i} = k_{\mathrm{cont}}\left(\mathbf{N}_{c_i}\mathbf{q}_{\mathrm{sys.kn}}^{t} - w_{\mathrm{irr}.c_i}\right) \quad , \quad F_{d_i} = \mathbf{k}_{\mathrm{d}.d_i}\mathbf{n}_{\mathrm{d}.d_i}\mathbf{q}_{\mathrm{sys.kn}}^{t}, \tag{A.9}$$

where vector $\mathbf{N}_{c_i}$ is the contribution of shape functions to the interpenetration at the c_ith contact position, $\mathbf{k}_{\mathrm{d}.i}$ is the stiffness matrix of the slackened dropper, $\mathbf{n}_{\mathrm{d}.i}$ is a boolean vector to select the coordinates at both ends of the ith dropper and $\mathbf{I}_n$ is a $n \times n$ identity matrix.

Appendix B. OCL-pantograph interaction model validation results

See Tables 6 and 7.

References

[1] Stefano Derosa, Petter Nåvik, Andrea Collina, Giuseppe Bucca, Anders Rønnquist, A heuristic wear model for the contact strip and contact wire in pantograph – Catenary interaction for railway operations under 15 kV 16.67 Hz AC systems, Wear (2020) 456–457, http://dx.doi.org/10.1016/j.wear.2020.203401.

[2] Giuseppe Bucca, Andrea Collina, A procedure for the wear prediction of collector strip and contact wire in pantograph–catenary system, Wear 266 (1–2) (2009) 46–59, http://dx.doi.org/10.1016/j.wear.2008.05.006.

[3] Mehdi Brahimi, Kamal Medjaher, Mohammed Leouatni, Noureddine Zerhouni, Prognostics and health management for an overhead contact line system - A review, Int. J. Progn. Health Manage. 8 (Special Issue 7) (2017) 1–16, http://dx.doi.org/10.36001/ijphm.2017.v8i3.2665.

[4] Chul Jin Cho, Hanseok Ko, Video-based dynamic stagger measurement of railway overhead power lines using rotation-invariant feature matching, IEEE Trans. Intell. Transp. Syst. 16 (3) (2015) 1294–1304, http://dx.doi.org/10.1109/TITS.2014.2361647.

[5] Marco Bocciolone, Giuseppe Bucca, Andrea Collina, Lorenzo Comolli, Design and testing of fibre Bragg grating force transducers for the measurement of pantograph–catenary contact force, Proc. Inst. Mech. Eng. F 233 (4) (2019) 396–409, http://dx.doi.org/10.1177/0954409718795762.

[6] Dongkai Zhang, Shibin Gao, Long Yu, Gaoqiang Kang, Dong Zhan, Xiaoguang Wei, A robust pantograph-catenary interaction condition monitoring method based on deep convolutional network, IEEE Trans. Instrum. Meas. 69 (5) (2020) 1920–1929, http://dx.doi.org/10.1109/TIM.2019.2920721.

[7] Dong Zhan, Deyan Jing, Mingli Wu, Dongkai Zhang, Long Yu, Tanglong Chen, An accurate and efficient vision measurement approach for railway catenary geometry parameters, IEEE Trans. Instrum. Meas. 67 (12) (2018) 2841–2853, http://dx.doi.org/10.1109/TIM.2018.2830862.

[8] Marco Bocciolone, Giuseppe Bucca, Andrea Collina, Lorenzo Comolli, Application of new optical load cells for in-line measurement of pantograph–catenary contact force, in: Fifth European Workshop on Optical Fibre Sensors, Vol. 8794 (May 2013), 2013, 879442, http://dx.doi.org/10.1117/12.2025853.

[9] Marco Bocciolone, Giuseppe Bucca, Alfredo Cigada, Andrea Collina, Lorenzo Comolli, An application of FBG accelerometers for monitoring pantographs of underground trains, in: Fourth European Workshop on Optical Fibre Sensors, Vol. 7653 (September 2010), 2010, 765341, http://dx.doi.org/10.1117/12.866358.

[10] Marco Carnevale, Andrea Collina, Processing of collector acceleration data for condition-based monitoring of overhead lines, Proc. Inst. Mech. Eng. F 230 (2) (2014) 472–485, http://dx.doi.org/10.1177/0954409714545637.

[11] Yang Song, Zhigang Liu, Xiaobing Lu, Dynamic performance of high-speed railway overhead contact line interacting with pantograph considering local dropper defect, IEEE Trans. Veh. Technol. 69 (6) (2020) 5958–5967, http://dx.doi.org/10.1109/TVT.2020.2984060.

[12] Yang Song, Anders Rønnquist, Tengjiao Jiang, Petter Nåvik, Identification of short-wavelength contact wire irregularities in electrified railway pantograph–catenary system, Mech. Mach. Theory 162 (2021) 104338, http://dx.doi.org/10.1016/j.mechmachtheory.2021.104338.

[13] Hongrui Wang, Zhigang Liu, Alfredo Nunez, Rolf Dollevoet, Entropy-based local irregularity detection for high-speed railway catenaries with frequent inspections, IEEE Trans. Instrum. Meas. 68 (10) (2018) 3536–3547, http://dx.doi.org/10.1109/TIM.2018.2881529.

[14] Hongrui Wang, Alfredo Núñez, Zhigang Liu, Yang Song, Fuchuan Duan, Rolf Dollevoet, Analysis of the evolvement of contact wire wear irregularity in railway catenary based on historical data, Veh. Syst. Dyn. 3114 (2017) 1–26, http://dx.doi.org/10.1080/00423114.2017.1408919.

[15] EN50318, Railway applications. Current collection systems. Validation of simulation of the dynamic interaction between pantograph and overhead contact line, 2018.

[16] A. Collina, A. Lo Conte, M. Carnevale, Effect of collector deformable modes in pantograph–catenary dynamic interaction, Proc. Inst. Mech. Eng. F 223 (1) (2009) 1–14, http://dx.doi.org/10.1243/09544097JRRT212.

[17] Yang Song, Anders Rønnquist, Petter Nåvik, Assessment of the high-frequency response in railway pantograph-catenary interaction based on numerical simulation, IEEE Trans. Veh. Technol. 69 (10) (2020) 10596–10605, http://dx.doi.org/10.1109/TVT.2020.3015044b.

[18] Olivier Vo Van, Introduction of variability into pantograph–catenary dynamic simulations, 2016.

[19] Jian Zhang, Wenzheng Liu, Zongfang Zhang, Study on characteristics location of pantograph-catenary contact force signal based on wavelet transform, IEEE Trans. Instrum. Meas. 68 (2) (2019) 402–411, http://dx.doi.org/10.1109/TIM.2018.2851422.

[20] Christopher Torrence, Gilbert P. Compo, A practical guide to wavelet analysis, Bull. Am. Meteorol. Soc. 79 (1) (1998) 61–78.

[21] Maria Molodova, Zili Li, Alfredo Núñez, Rolf Dollevoet, Automatic detection of squats in railway infrastructure, IEEE Trans. Intell. Transp. Syst. 15 (5) (2014) 1980–1990, http://dx.doi.org/10.1109/TITS.2014.2307955.

[22] Ebru Karakose, Muhsin Tunay Gencoglu, Mehmet Karakose, Ilhan Aydin, Erhan Akin, A new experimental approach using image processing-based tracking for an efficient fault diagnosis in pantograph–catenary systems, IEEE Trans. Ind. Inf. 13 (2) (2017) 635–643, http://dx.doi.org/10.1109/TII.2016.2628042.

[23] Xuan Yang, Ning Zhou, Yueping Liu, Wei Quan, Xuemin Lu, Weihua Zhang, Online pantograph–catenary contact point detection in complicated background based on multiple strategies, IEEE Access 8 (2020) 220394–220407, http://dx.doi.org/10.1109/ACCESS.2020.3042535.

[24] Frank Hutter, Lars Kotthoff, Joaquin Vanschoren, Automated Machine Learning, in: The Springer Series on Challenges in Machine Learning, Springer Nature, Cham, 2019, http://dx.doi.org/10.1007/978-3-030-05318-5.

[25] Livia Faes, Siegfried K. Wagner, Dun Jack Fu, Xiaoxuan Liu, Edward Korot, Joseph R. Ledsam, Trevor Back, Reena Chopra, Nikolas Pontikos, Christoph Kern, Gabriella Moraes, Martin K. Schmid, Dawn Sim, Konstantinos Balaskas, Lucas M. Bachmann, Alastair K. Denniston, Pearse A. Keane, Automated deep learning design for medical image classification by health-care professionals with no coding experience: a feasibility study, Lancet Digit. Health 1 (5) (2019) e232–e242, http://dx.doi.org/10.1016/S2589-7500(19)30108-6.
[26] Hongrui Wang, Alfredo Nunez, Zhigang Liu, Dongliang Zhang, Rolf Dollevoet, A Bayesian network approach for condition monitoring of high-speed railway catenaries, IEEE Trans. Intell. Transp. Syst. (August) (2019) 1–15, http://dx.doi.org/10.1109/tits.2019.2934346.
[27] Elton F. de S. Soares, Carlos Alberto V. Campos, Sidney C. de Lucena, Online travel mode detection method using automated machine learning and feature engineering, Future Gener. Comput. Syst. 101 (2019) 1201–1212, http://dx.doi.org/10.1016/j.future.2019.07.056.
[28] Stefano Bruni, Jorge Ambrosio, Alberto Carnicero, Yong Hyeon Cho, Mitsuru Ikeda, Sam Young Kwon, Jean-pierre Massat, Manuel Tur, Weihua Zhang, Stefano Bruni, Jorge Ambrosio, Alberto Carnicero, Yong Hyeon Cho, Mitsuru Ikeda, Sam Young Kwon, Jean-pierre Massat, Sebastian Stichel, Manuel Tur, The results of the pantograph – catenary interaction benchmark, Veh. Syst. Dyn. 53 (3) (2015) 412–435, http://dx.doi.org/10.1080/00423114.2014.953183.
[29] Jong Hwi Seo, Seok Won Kim, Il Ho Jung, Tae Won Park, Jin Yong Mok, Young Guk Kim, Jang Bom Chai, Dynamic analysis of a pantograph–catenary system using absolute nodal coordinates, Veh. Syst. Dyn. 44 (8) (2006) 615–630, http://dx.doi.org/10.1080/00423110500373721.
[30] M. Tur, E. García, L. Baeza, F.J. Fuenmayor, A 3D absolute nodal coordinate finite element model to compute the initial configuration of a railway catenary, Eng. Struct. 71 (2014) 234–243, http://dx.doi.org/10.1016/j.engstruct.2014.04.015.
[31] Yang Song, Pedro Antunes, Joao Pombo, Zhigang Liu, A methodology to study high-speed pantograph–catenary interaction with realistic contact wire irregularities, Mech. Mach. Theory (ISSN: 0094-114X) 152 (2020) 103940, http://dx.doi.org/10.1016/j.mechmachtheory.2020.103940.
[32] C. Sánchez-Rebollo, A. Carnicero, J.R. Jiménez-Octavio, CANDY Statement of methods, Veh. Syst. Dyn. 53 (3) (2015) 392–401, http://dx.doi.org/10.1080/00423114.2014.982135.
[33] Yong Hyeon Cho, SPOPS Statement of methods, Veh. Syst. Dyn. 53 (3) (2015) 329–340, http://dx.doi.org/10.1080/00423114.2014.953182.
[34] Mitsuru Ikeda, 'Gasen-do FE' Statement of methods, Veh. Syst. Dyn. 53 (3) (2015) 357–369, http://dx.doi.org/10.1080/00423114.2014.968174.
[35] Santiago Gregori, Manuel Tur, José Enrique Tarancón, Francisco Javier Fuenmayor, Stochastic Monte Carlo simulations of the pantograph–catenary dynamic interaction to allow for uncertainties introduced during catenary installation, Veh. Syst. Dyn. 57 (4) (2019) 471–492, http://dx.doi.org/10.1080/00423114.2018.1473617.
[36] CEN-CENELEC, EN-50367 Railway applications - current collection systems - technical criteria for the interaction between pantograph and overhead line (to achieve free access), 2012.
[37] S. Gregori, M. Tur, E. Nadal, J.V. Aguado, F.J. Fuenmayor, F. Chinesta, Fast simulation of the pantograph–catenary dynamic interaction, Finite Elem. Anal. Des. 129 (2016) (2017) 1–13, http://dx.doi.org/10.1016/j.finel.2017.01.007.
[38] Olivier Vo Van, Etienne Balmés, Arnaud Capitaine, Xavier Lorang, Sensitivity analysis of catenary geometry on current collection quality, in: The Third International Conference on Railway Technology: Research, Development and Maintenance; Cagliari, Italy; 2016, 2016, http://dx.doi.org/10.4203/ccp.110.108.
[39] Chayut Ngamkhanong, Sakdirat Kaewunruen, Charalampos Baniotopoulos, Far-field earthquake responses of overhead line equipment (OHLE) structure considering soil–structure interaction, Front. Built Environ. 4 (2018) 35, http://dx.doi.org/10.3389/fbuil.2018.00035.
[40] H2O.ai. H2O-automl: Manual, 2020. 3.30.0.1.
[41] David H. Wolpert, Stacked generalization, Neural Netw. 5 (2) (1992) 241–259, http://dx.doi.org/10.1016/S0893-6080(05)80023-1.
[42] Takaya Saito, Marc Rehmsmeier, The precision-recall plot is more informative than the ROC plot when evaluating binary classifiers on imbalanced datasets, PLoS One 10 (3) (2015) e0118432, http://dx.doi.org/10.1371/JOURNAL.PONE.0118432.